Analysis Note for draft paper titled:

Coulomb effect in $Au_{like} + Al$ collisions at $\sqrt{s_{NN}} = 3.0,\ 3.5,\ \text{and}\ 4.5$ GeV

B. A. Haag[1], C. E. Flores[1], S. G. Brovko[1], J. E. Draper[1],

J. L. Romero[1], G. Odyniec[2], R. Witt[3], D. Cebra[1]

(Principle Authors)

J. deAnda[1], I. Domagalski[1], J. Rives[1]

(Special one paper authors)

[1] *University of California, Davis, California 95616*

[2] *Lawrence Berkeley National Laboratory, Berkeley, California 94720*

[3] *United States Naval Academy, Annapolis, Maryland 21402*

(Dated: November 15, 2015)

Abstract

The first results of fixed-target heavy-ion collisions at RHIC using the STAR detector are presented. An analysis of the transverse mass spectra of midrapidity pions and protons from central Au+Al (beam-pipe) collisions at $\sqrt{s_{NN}} = 3.0,\ 3.5$ and 4.5 GeV has been performed. Slope parameters using an exponential fit function were extracted from the spectra and used to determine the Coulomb potential from the pion ratio. Additionally, acceptances for tracking in the TPC are discussed. The results of this analysis are presented and compared to previous results from experiments at the AGS, SPS, and RHIC.

CONTENTS

I. MOTIVATION

The Beam Energy Scan (BES) at RHIC was designed to study the nature of the phase transition between hadronic and partonic nuclear matter. In particular, it was proposed to search for the critical point between the two phases. There is some evidence which suggests that deconfinement has been achieved in the low energy range of the BES. However, there are

several dynamical model simulations which suggest that the partonic phase may be entered for center of mass energies as low as 4 to 5 GeV.

The study of such low energy collisions is not possible using RHIC in the "collider mode. Hence, it is necessary to study fixed-target collisions. This fixed-target system is achieved by studying collisions between the gold beam-halo and the aluminum beampipe in the STAR detector. Colliding systems with center-of-mass energies of 7.7, 11.5, and 11.5 GeV (Single Gold beams with kinetic energies of 2.9, 4.8, and 8.8 AGeV) result in $Au + Al$ collisions at center-of-mass energies of 3.0, 3.5, and 4.5 GeV respectively
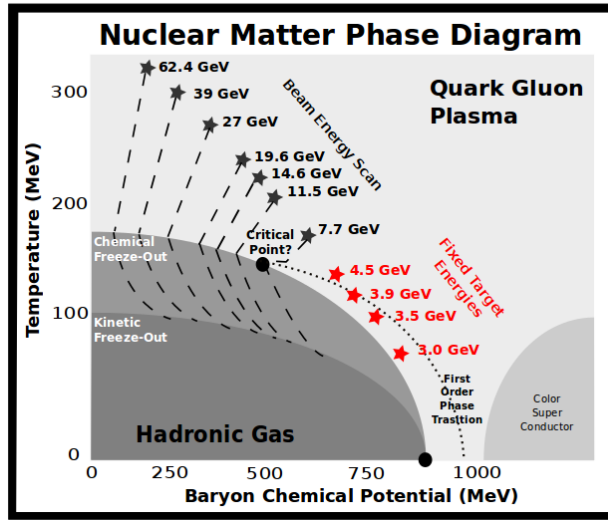

FIG. 1. (1.1) Phase Diagram

II.   FIXED-TARGET BASICS

STAR was built to measure symmetric collisions of separate particle beams, but never intended to measure collisions with fixed-targets. By analyzing the data from the ion beam with the beam pipe material, Al, we are pushing the absolute limits of STAR's capability. An example of a reconstructed fixed target collision is illustrated in leftmost figure below. Figure 2.1 shows an example of a fixed-target collision as measured in the STAR detector. The black rings denote the endcaps of the TPC, the yellow horizontal line represents the beam line, the red vertical line illustrates the position of the central membrane and all the blue and cyan lines are reconstructed tracks where the darker shade represents the part of the track which is extrapolated from the helical fit to the hit points (the lighter shade). As

you can see, all of the tracks are directed asymmetrically to one side of the detector, not distributed in the forward and backward regions as one would expect for a colliding beam event.

In order to ensure that tracks are long and obtain plenty of hit points for decent resolution and dE/dx measurements we need to look at the z position of the vertex, V_z, displaced from the center of the detector, and in fact look at the region from 150 cm $< |V_z| <$ 200 cm. When we select for events with this displaced vertex position we have a different geometry for detector acceptance. This geometry is illustrated in figure 2.2. All detector subsystems are labeled in the diagram, as well as the aluminum portions of the beam pipe in green and the beryllium portion in blue. Also in green are sample tracks that illustrate the pseudorapidity acceptance of the TPC and TOF for an event with a vertex at the very edge of the detector.

For the BES energies that we can analyze a significant number of events to obtain particle spectra the highest mid-rapidity we have is $y_{mid} = 1.52$ for the $\sqrt{s_{NN}} = 4.5$ GeV energy. These data were collected during the $\sqrt{s_{NN}} = 19.6$ GeV energy beams. It is important to note that for the highest energy, we begin losing acceptance in the forward region but have full acceptance from beam rapidity back to target rapidity. For the other energies, we have some acceptance in the forward region, but full acceptance from beam rapidity back to target rapidity.

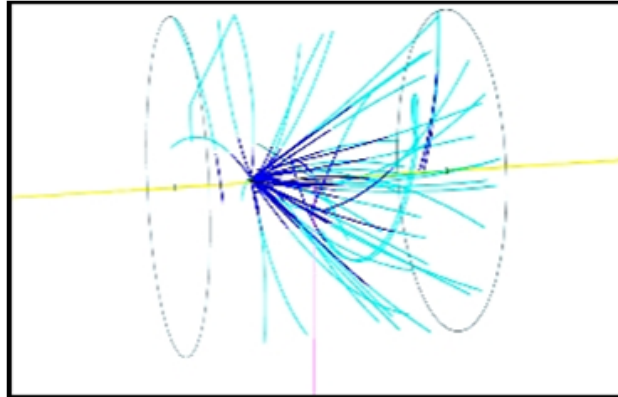Figure 2.3 below shows a UrQMD simulation of a fixed-target event in the STAR detector.
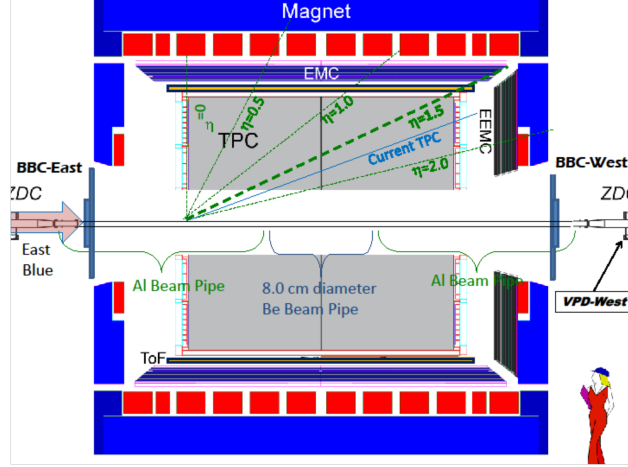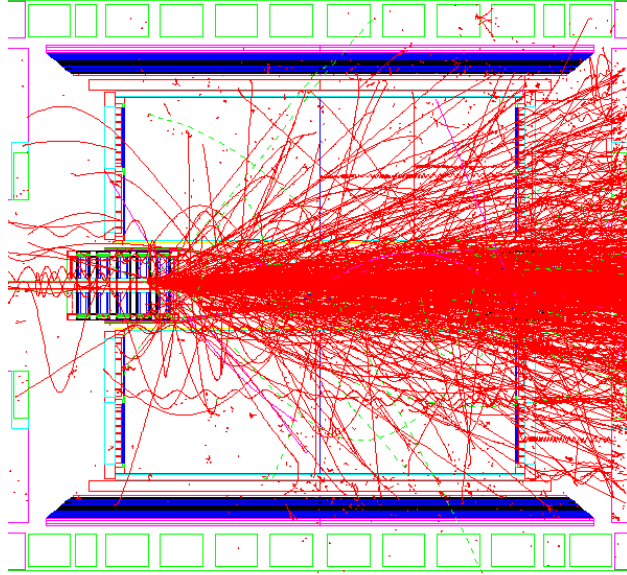

FIG. 2. (2.1)

FIG. 3. (2.2)

FIG. 4. (2.3)

III.   DATA SETS

For the fixed-target analysis, there was no bad run selection. The logic for that decision was that the runs which might be throw away in the collider program for poor beam quality were exactly the runs which would have the highest background and therefore the most $Au + Al$ events. Data were analyzed for the full run list of each of the BES energies at or below injection energy. Events from the full data set were used to embed into, therefore the effeciencies should reflect the status of the detectors during the course of each run.

5

TABLE I. (3.1) FXT Data Sets

FXT (Gev)	Collider (GeV)	First Run	Last Run	Dates	FXT Events	Collider Events	Min Bias Triggers
3.0	7.7	11114074	11147022	4/24 to 5/27 2010	61589	4M	100M
3.5	11.5	11148001	11158044	5/28 to 6/07 2010	98402	12M	52M
3.9	14.5	15047102	15070021	2/17 to 3/11 2014	TBD	20M	206M
4.5	19.6	12113075	12122019	4/24 to 5/02 2011	44792	36M	83M

IV. EVENT SELECTION (ANALYSIS CUTS)

Macro: — StMuDstBeamPipeAnalysisMaker.cxx

Selection Criteria:

- Trigger == No Selection

- $150 \text{ cm} < |V_z| < 200 \text{ cm}$

- $2 \text{ cm} < V_r < 5 \text{ cm}$

- $\Sigma P_z > 0$

A total of four cuts are made before reaching the analyzed data sets two geometric vertex requirements, one dynamic requirement, and one centrality requirement. To ensure that only beampipe events are analyzed we require the radial position of the primary event vertex to satisfy $2 \leq V_r \leq 5$. Additionally, to ensure that tracks from the collision point will transverse a sufficient distance in the TPC for particle indentification we require the z-position of the primary event vertex to satisfy $150 \leq |V_z| \leq 200$ cm. These two geometric cuts are insuffienct for determining analyzable events. For example, they premit an event satisfying their conditions, but which is heading away from the TPC. To ensure that the events which pass the geometric cuts will transverse the TPC we require the total momentum of the tracks in an event to be positive. Finally, only the ten percent most central collisions are desired for the analysis. Thus, a centrality cut is made using the number of pions. For more on the method used to determine the centrality of the collisions see below.
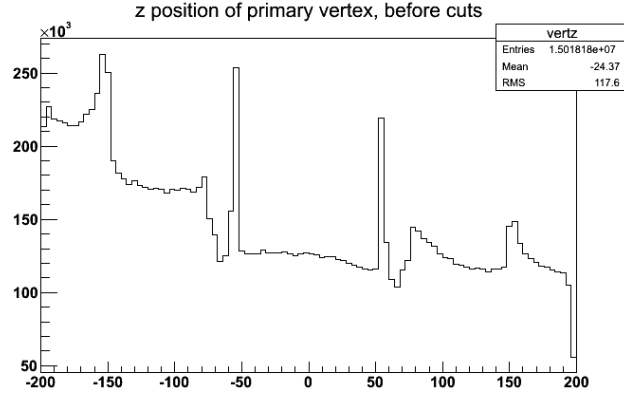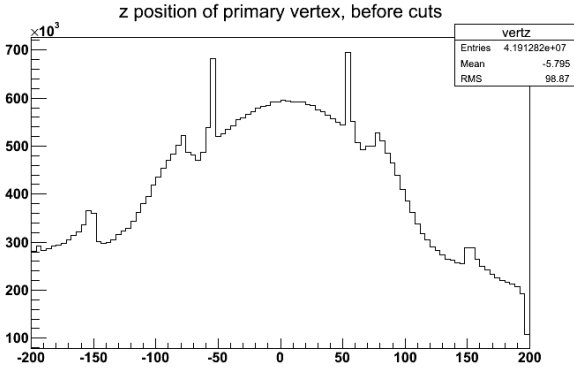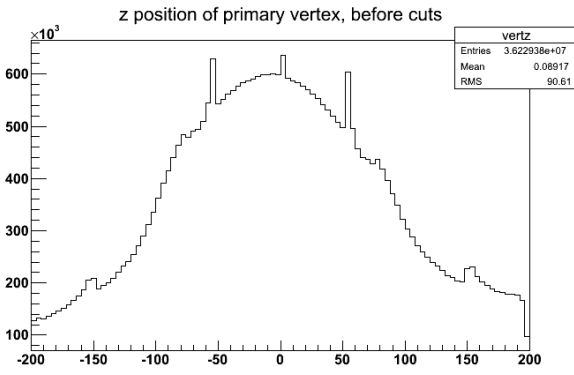
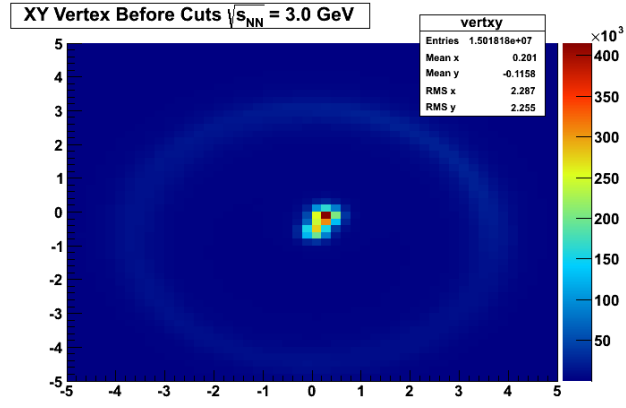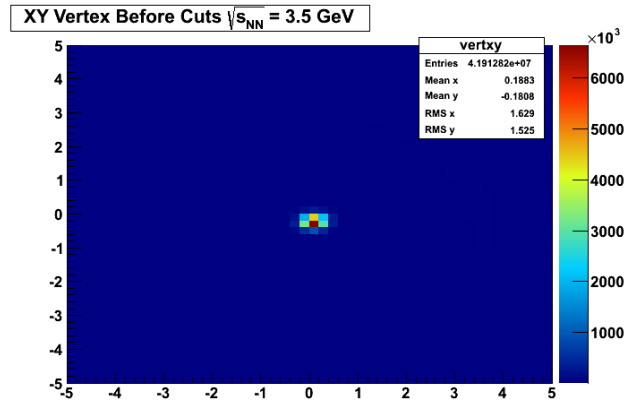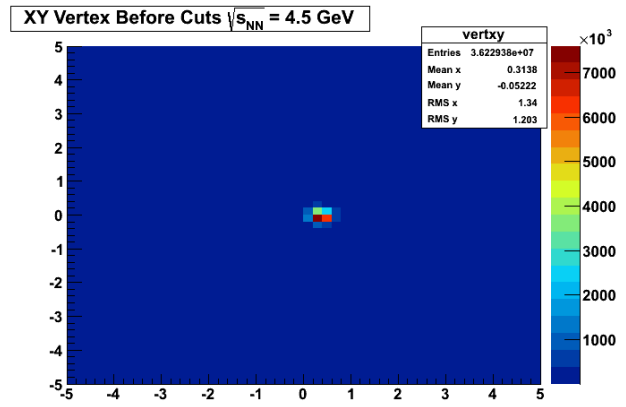FIG. 5. (4.1)

FIG. 6. (4.2)
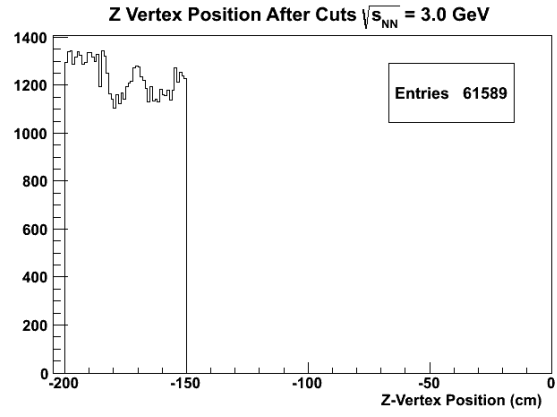

FIG. 7. (4.3)

FIG. 8. (4.4)
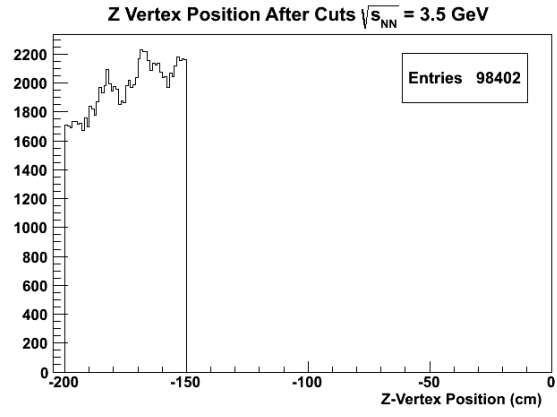

FIG. 9. (4.5)
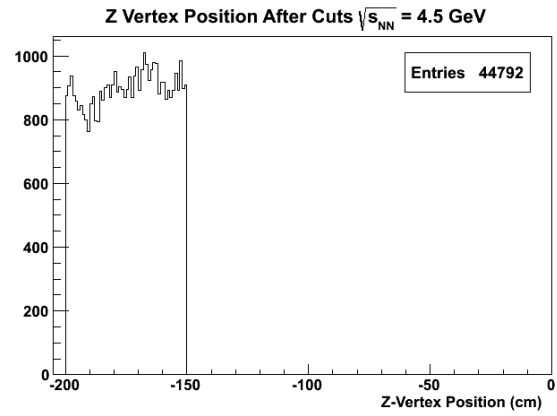

FIG. 10. (4.6)

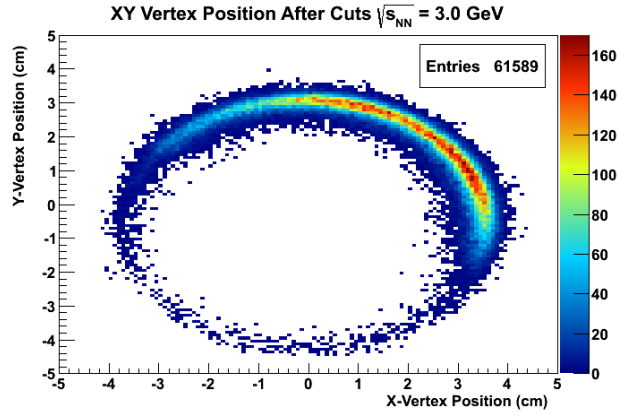FIG. 11. (4.7)

FIG. 12. (4.8)

FIG. 13. (4.9)

FIG. 14. (4.10)
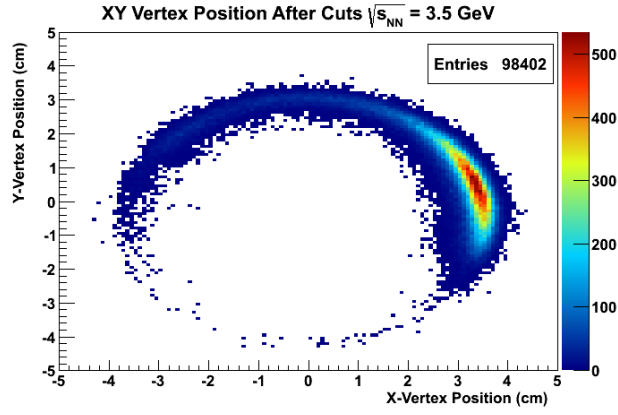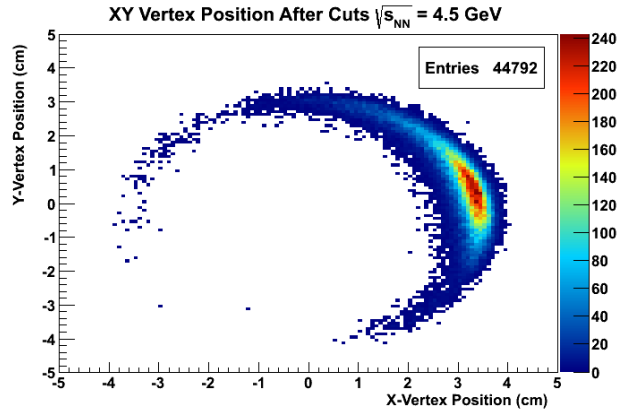

FIG. 15. (4.11)

FIG. 16. (4.12)

V. CENTRALITY SELECTION (ANALYSIS CUTS)

Selection Criterion: 0-10% most central

Another challenge of the fixed target collisions appears when attempting to determine centrality of $Au + Al$ to compare to other spectra. Recall that Al has 27 nucleons while Au has 197. As we recall, the nucleon density of the nucleus is uniform, and we can estimate the radius of the nucleus from it's volume and the number of nucleons: $R = R_0 A^{1/3}$ where $R_0 \simeq 1.2$ fm and A is of course the number of nucleons. Au has a radius of 6.97 fm and Al has a radius of 3.6 fm, as we can see in the figure below. This leads to a range of impact parameters where the Al nucleus is completely absorbed by the Au ion. We had to determine what "most central" would mean for this type of collision, and it largely depended on the number of participating Au nucleons.

FIG. 17. (5.1)

The centrality of the $Au + Al$ collision is determined by a Glauber Monte-Carlo model. Nucleons are randomly distributed according to a Woods-Saxon function for each nucleus. An impact parameter is randomly chosen and the transverse position of each of the nucleons is computed. The nucleons within the overlap region are counted as participant nucleons (N_{part}) and the number of nucleons impinging on the two dimensional area (cross-section) of a nucleon from the opposing nucleus are counted as having had a binary collision (N_{coll}).

$$f(k) = \frac{\Gamma(k+n)}{\Gamma(k+1)\Gamma(n)} \frac{(\mu/n)^k}{(1+\mu/n)^{n+k}} \tag{1}$$

where $\mu = \frac{np}{1-n}$

We have also considered what observable would best corrspond to centrality in these low energy fixed-target collisions. To address this question, we ran UrQMD simulations and applied cuts to simulate the acceptance of the TPC for fixed-target events. The results of
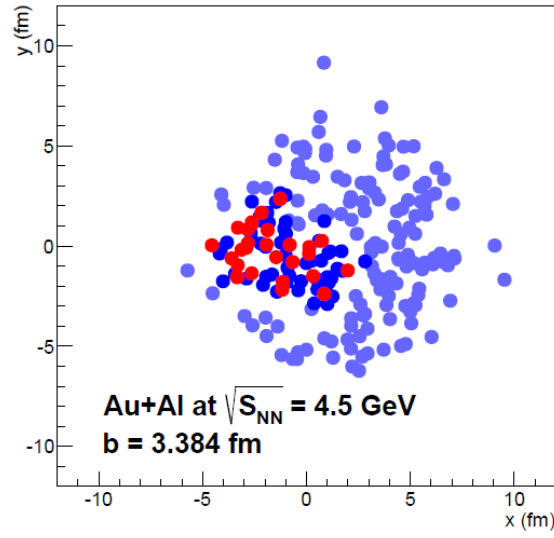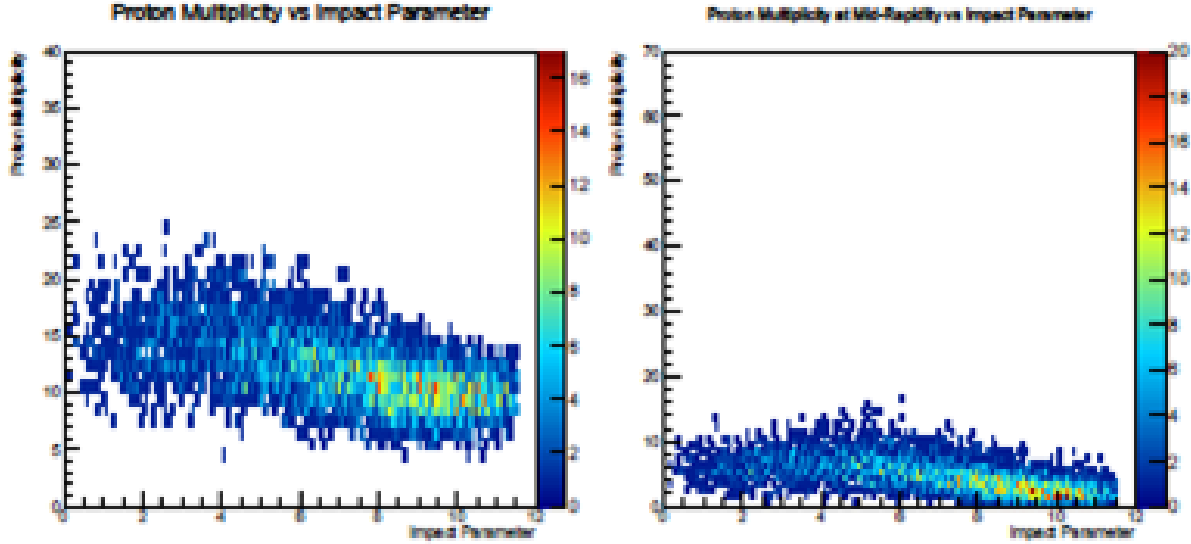
11

FIG. 18. (5.2)

these studies are shown below.

FIG. 19. (5.3 and 5.4)

Pion production is modeled with the Negative Binomial Distribution (NBD) above. For each $Au+Al$ collision the NBD is sampled N_{part} number of times. The parameters n and p of the NBD are determined using a grid search method looping through various combinations of the parameters and performing a χ^2 test each time until an acceptable χ^2 was found. The pion multiplicities for many $Au+Al$ Glauber Monte-Carlo collisions were agregated and the

12

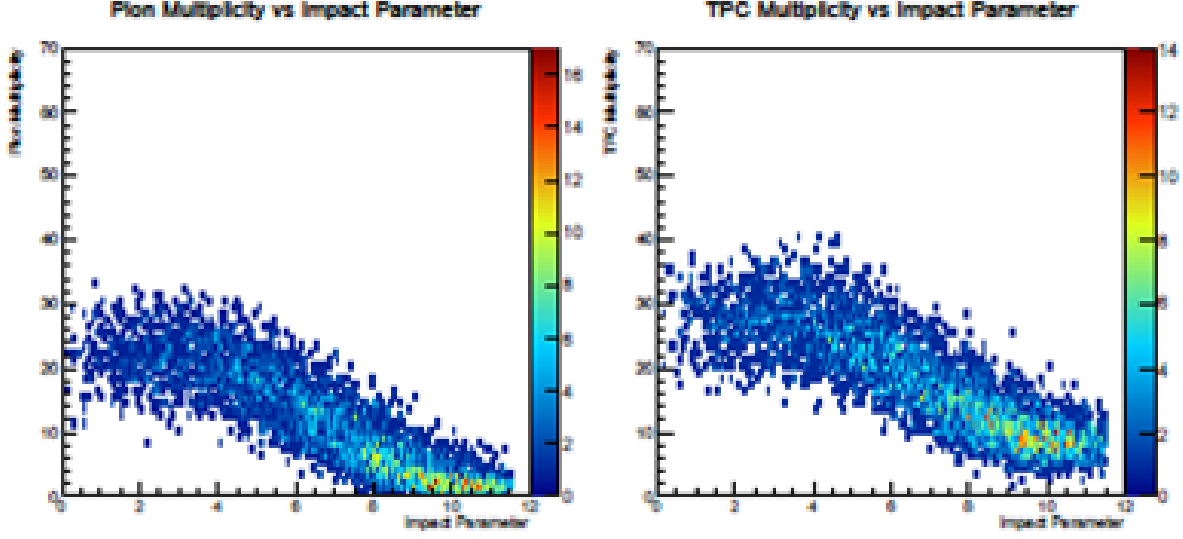FIG. 20. (5.5 and 5.6)

1 pion multiplicty distribution was integrated to find the pion multiplicity coressponding to
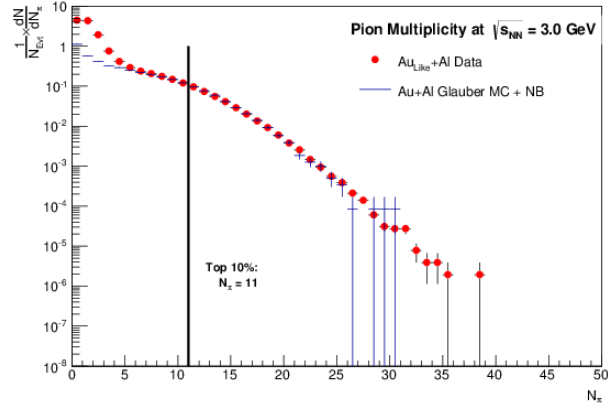2 the top ten percent.

FIG. 21. (5.7)
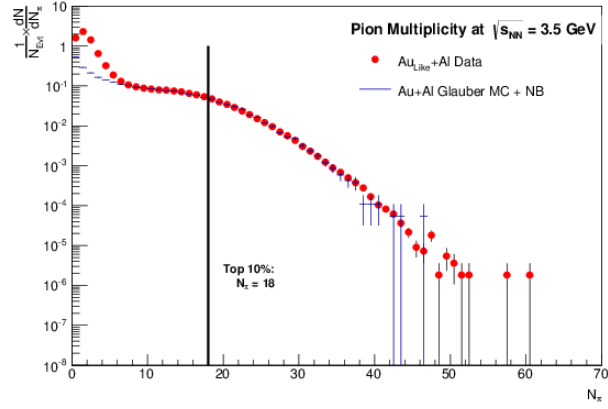
FIG. 22. (5.8)

TABLE II. (5.1) The extracted Coulomb potential (V_C) and initial pion ratio (R_i) are tabulated for each bombarding energy. Statistical and systematic errors are listed.

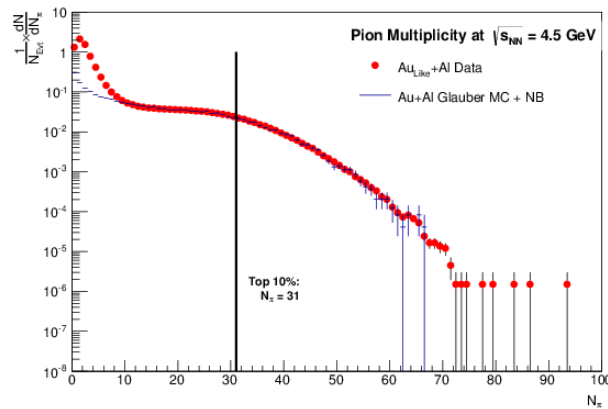| $\sqrt{s_{NN}}$ (GeV)	$V_C\|_{y=0}$ (MeV)	$R_i\|_{y=0}$
3.0	$12.1 \pm 1.1 \pm 1.5$	$0.81 \pm .06 \pm .08$
3.5	$9.1 \pm 0.9 \pm 0.6$	$0.85 \pm .05 \pm .03$
4.5	$7.5 \pm 1.5 \pm 1.9$	$0.90 \pm .07 \pm .03$

FIG. 23. (5.9)

14

VI. TRACK SELECTION (ANALYSIS CUTS)

- dca.mag() = we use the 2 cm cut for primary tracks that is implicit in the tracker

- hHits() = we use the 5 hit cut that is implicit as the minimum seed length

- nHitsFit()/nHitsPoss() ¿ 0.52

- nHitsDedx() = none

Because the fixed-target geometry focuses mid-rapidity tracks forward, it was necessary to keep the track cuts as open as possible. Therefore, essentially our only track quality cut was the fraction of possibile hits. We kept this at the standard 0.52 to avoid the possibilities of split tracks. We did not employ a cut on the number of hits as we did not want to limit the forward rapidity in software, we wanted to extend the analysis to the limits of the hardware.
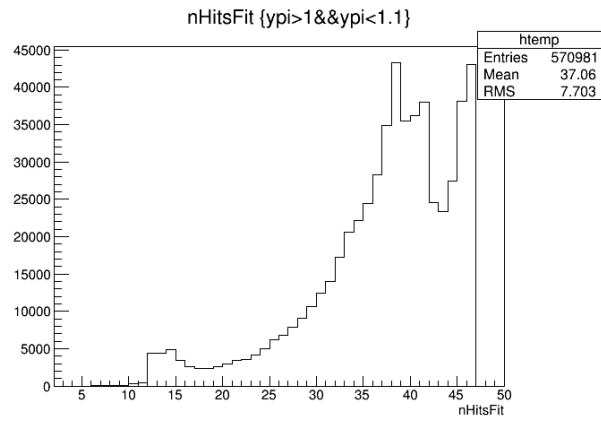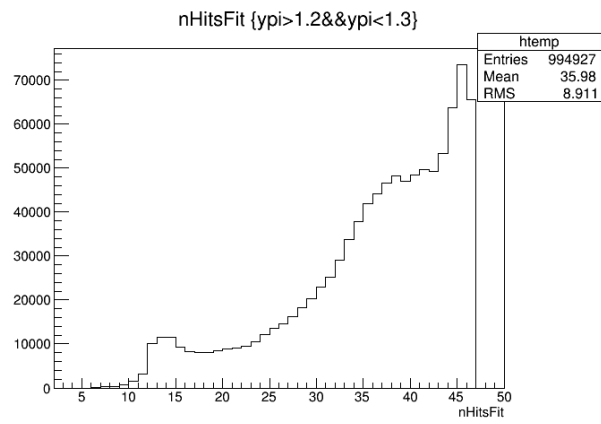
FIG. 24. (6.1)

FIG. 25. (6.2)
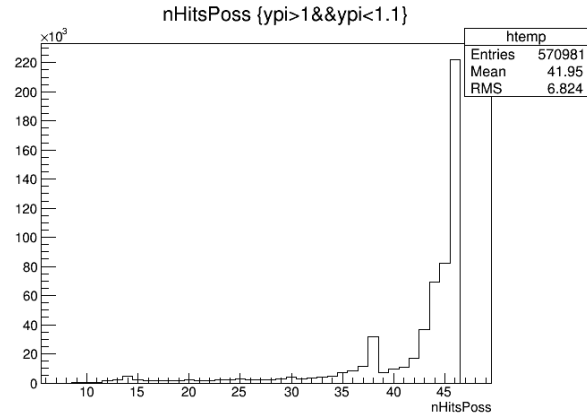
FIG. 27. (6.4)
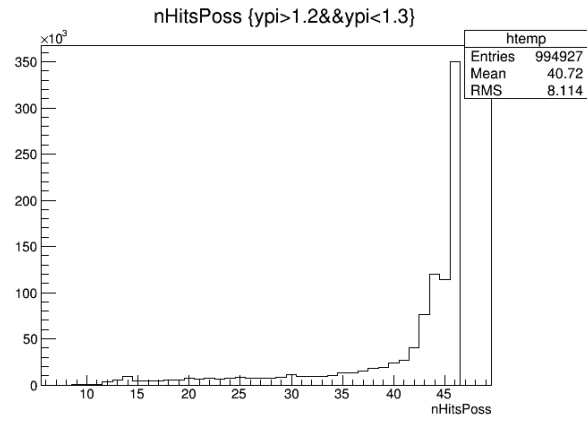
FIG. 28. (6.5)
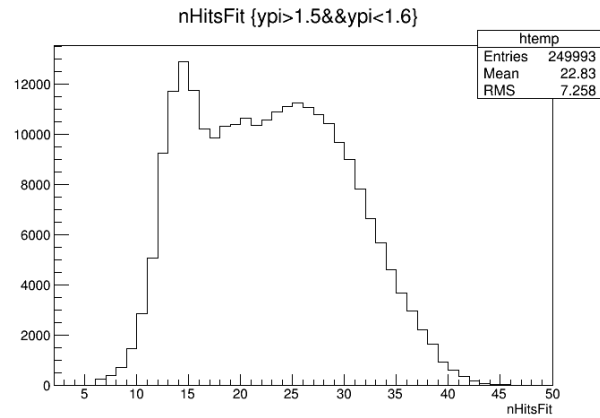
FIG. 26. (6.3)
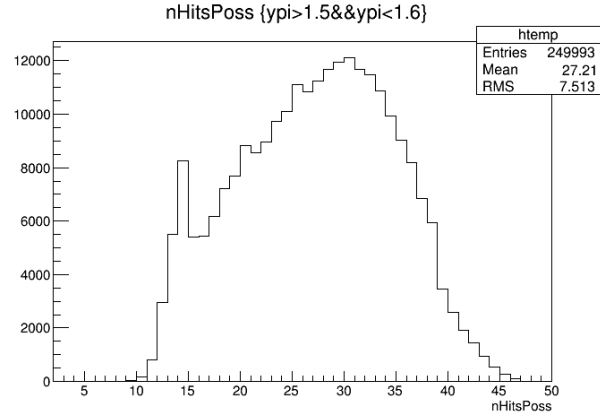
FIG. 29. (6.6)
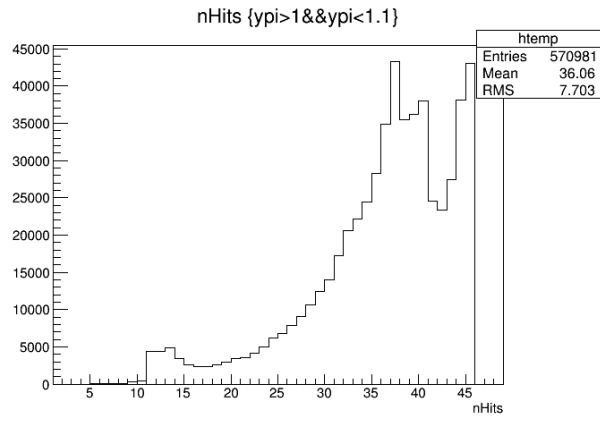
FIG. 30. (6.7)
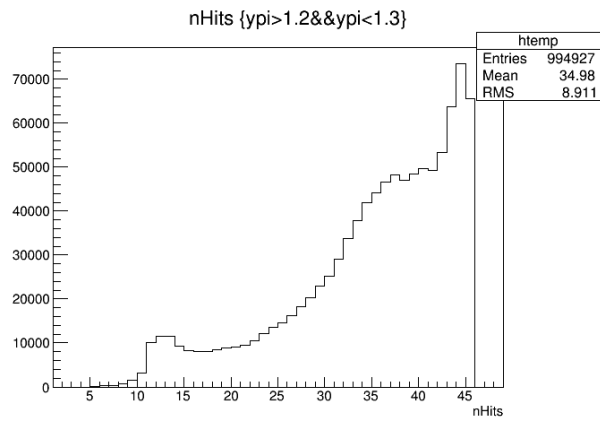
FIG. 31. (6.8)
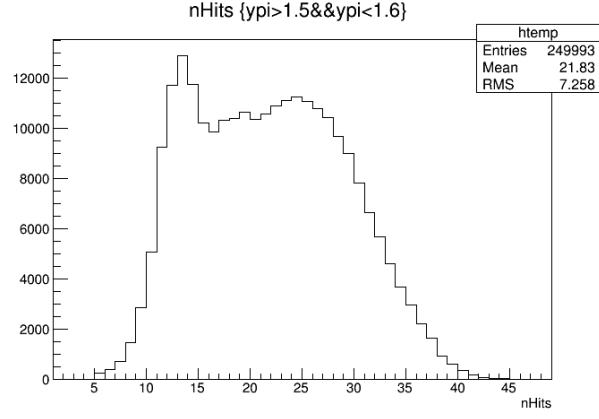
FIG. 32. (6.9)
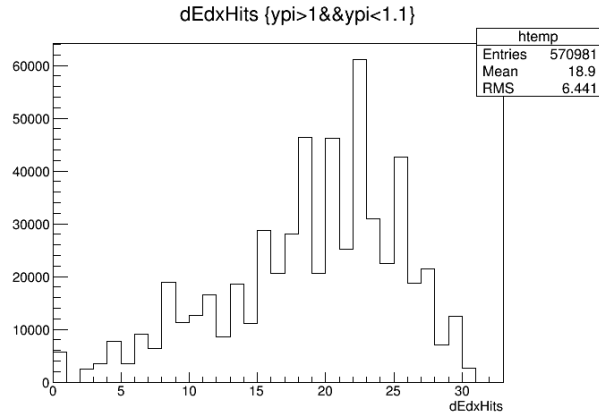
FIG. 33. (6.10)
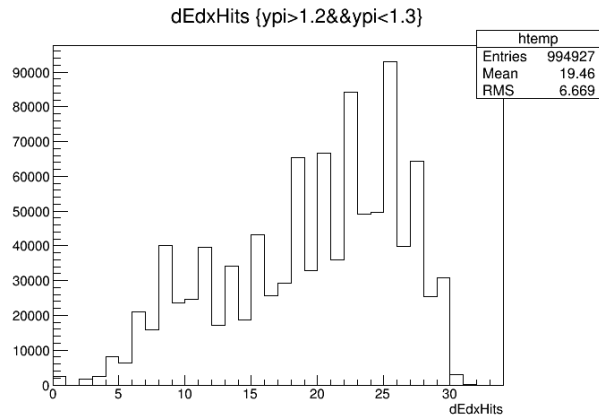
FIG. 34. (6.11)
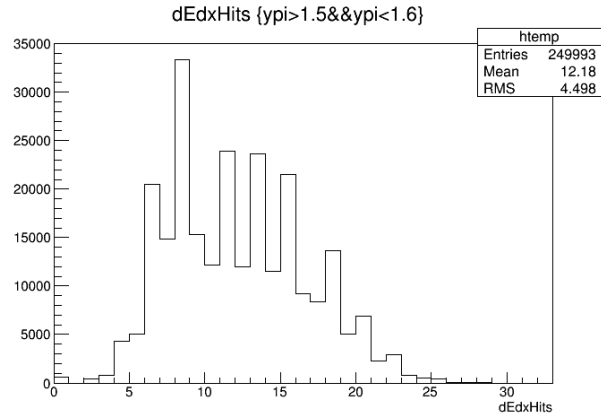
FIG. 35. (6.12)

FIG. 36. (6.13)

FIG. 37. (6.14)

dcaD {ypi>1.5&&ypi<1.6}

htemp	
Entries	249993
Mean	0.04489
RMS	0.8393

FIG. 38. (6.15)

dcaZ {ypi>1&&ypi<1.1}

htemp	
Entries	570981
Mean	-0.003449
RMS	0.584

FIG. 39. (6.16)

dcaZ {ypi>1.2&&ypi<1.3}

htemp	
Entries	994927
Mean	0.001171
RMS	0.5374

FIG. 40. (6.17)

dcaZ {ypi>1.5&&ypi<1.6}

htemp	
Entries	1249993
Mean	0.02958
RMS	0.4345
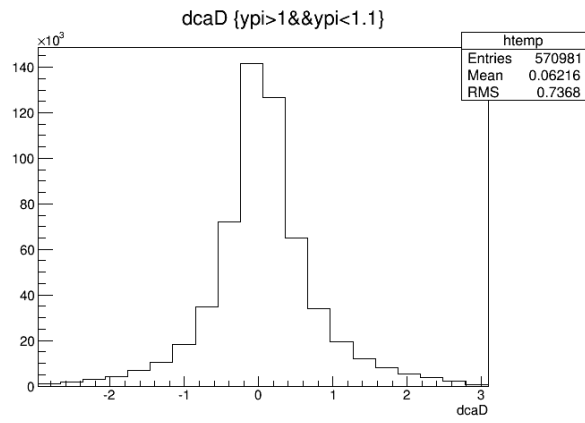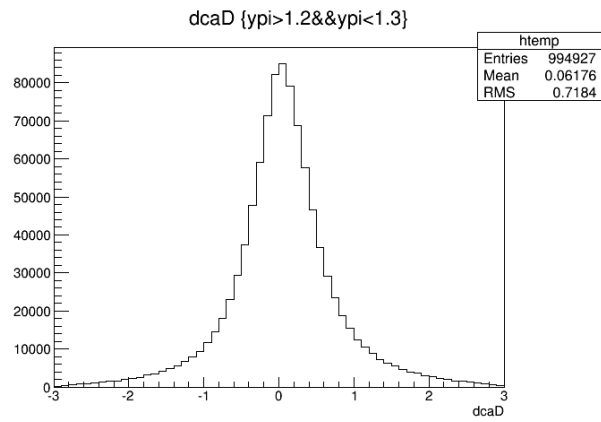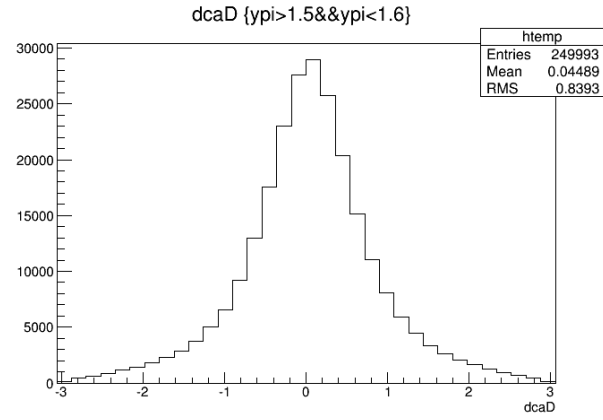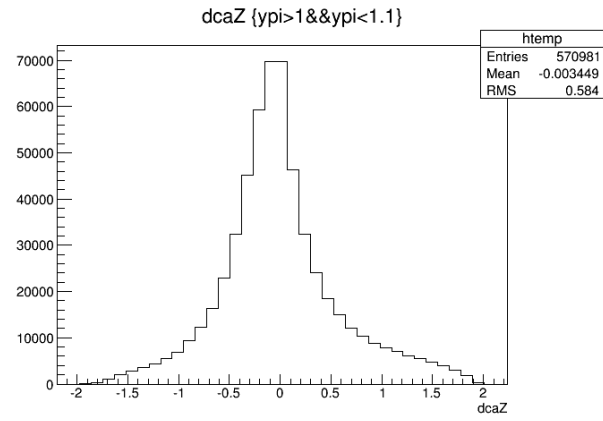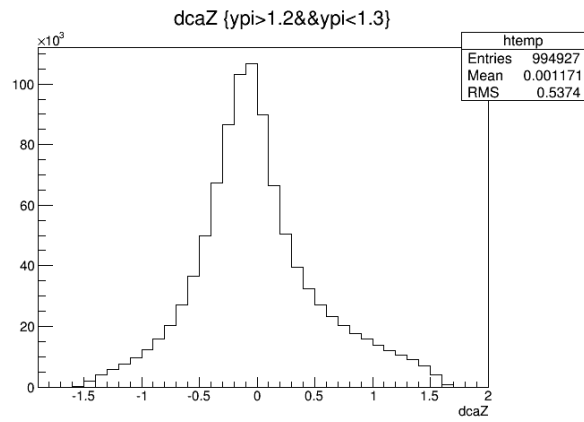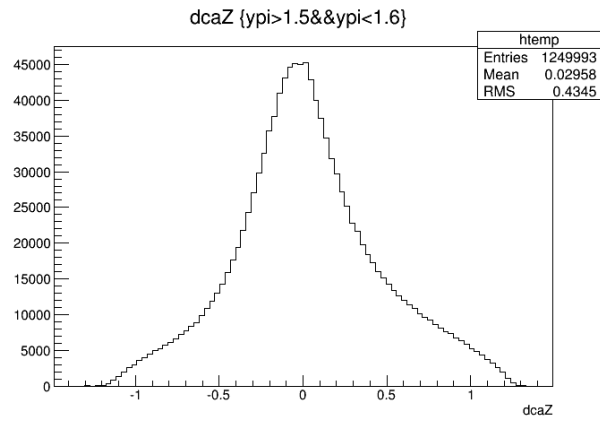
FIG. 41. (6.18)

VII.   ACCEPTANCE IN FXT MODE

When changing beam energy in the accelerator, the acceptance of the detector changes as well. This is a feature of a fixed target experiment. Particle acceptances can be seen in the two figures below with pions on the left and protons on the right. Note that as the energy of the beam changes, so does mid-rapidity and thus the acceptance of the detector. Pions have relatively uniform acceptance in this geometry. However, protons have a high cut-in that depends on the beam energy. This efficiency loss will affect the ability to obtain a spectrum in the low momentum region.
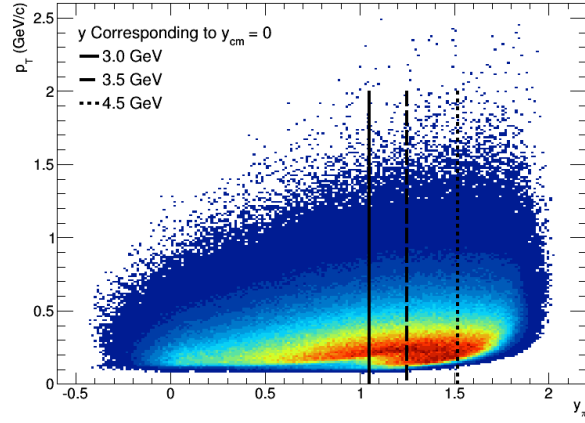
FIG. 42. (7.1)
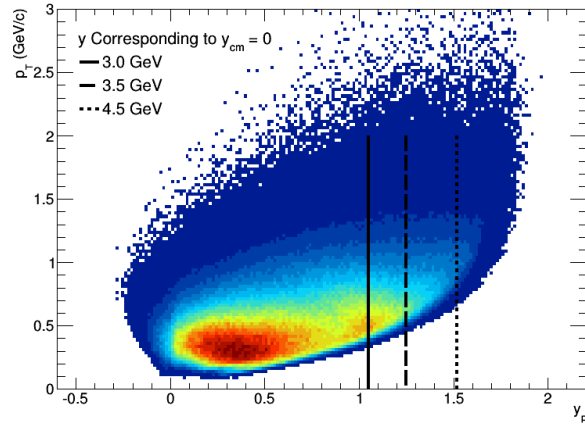
FIG. 43. (7.2)

VIII. PID PLOTS

Events satisfying the above cuts and their tracks are collected. The energy loss of each track as it transverses the TPC (dE/dx) is plotted as a function of the track momentum. It is clear from the dE/dx distributions that PID is possible in the fixed target configuration using the TPC. In Fig.s 8.1 to 8.3 The dE/dx is shown on a linear scale, which highlights the minimum ionizing particles. Superimposed on the intensity maps are the predicted centroids for each particle type as given by the Bichsel parameterization. One can easily pick out the bands identifying the electrons, pions, kaons, protons, deuterons, and tritons. One can also note that as the collision energy is increased there is an increase in the realtive yield of pions and kaons and a decrease in the relative yield of deuterons and tritons.

Figures 8.4 to 8.6 were made to illustrate the challenge of identifying protons in the fixed-target geometry. The figures now present dE/dx using a logrithmic scale. This shows more of the highly ionizing particles and now bands for the helions and alphas are clearly visible. In these figures, the intensity maps are first made allowing all rapidities to show the trends of the bands, then superimposed in magenta are tracks which would be within 0.05 units of mid-rapidity were they protons. Clearly the forward boost center-of-mass frame introduces some challenges that one does not have in a collider. The main challenge comes from the pions which are not distinguishable from the protons using dE/dx. We approach this problem using the same approach employed by the E895 experiment at the AGS. We measure the negative pions in identical selection criteria for each bin. The yield of positive and negative pions is not unity at these energies, however, one of the main points of this paper is to determine the pion ratios, and these ratios values are used to correctly scale the negative pions so that the positive pions admixture in the protons can be subtracted. One should note that there are neglibible contributions of anti-protons and K^- mixed into the π^-, and K^+ mixed into the protons. These figures just provides a big picture overview of the approach to getting clean proton spectra; the details are given in the next section (specifically figures 9.13 to 9.18, which show the Gaussian fits the the dE/dx distributions for each bin).
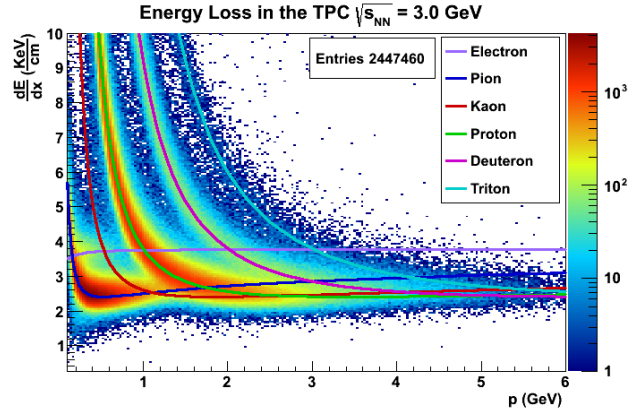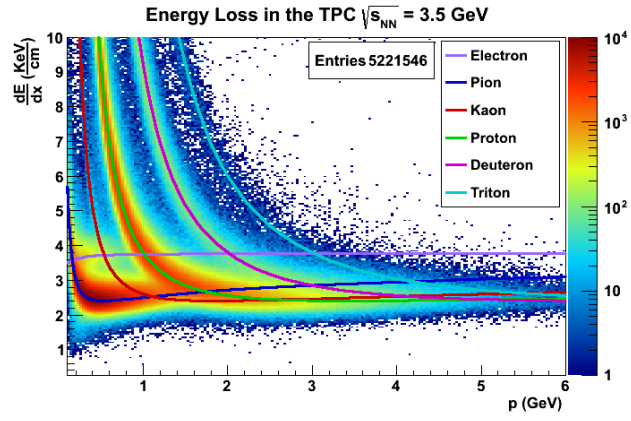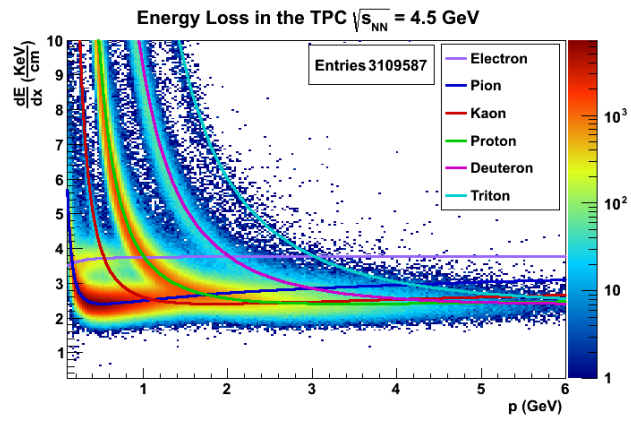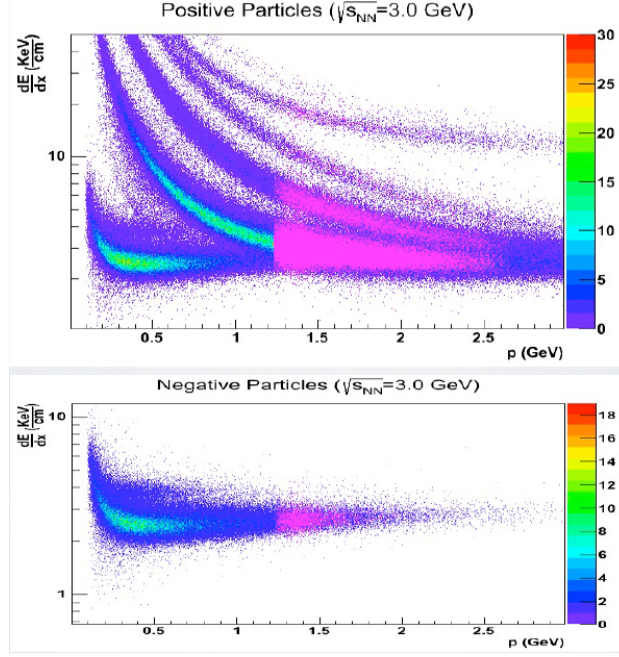
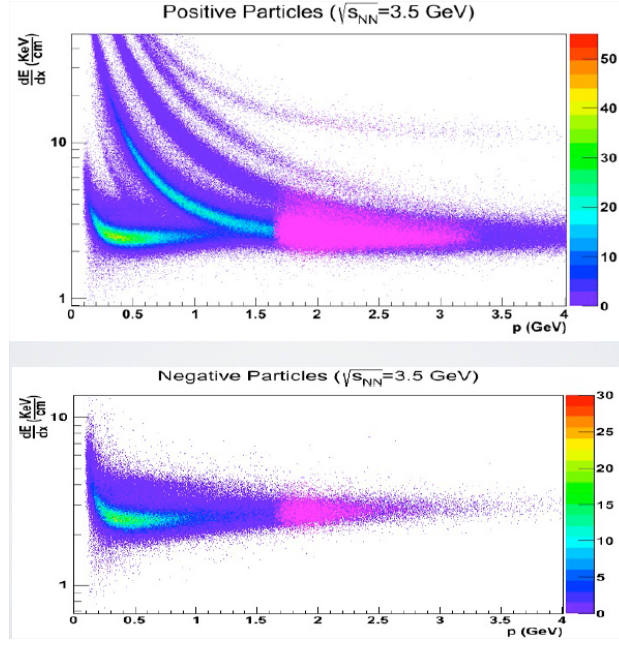24

FIG. 44.

FIG. 45.

FIG. 46.

25

FIG. 47.

FIG. 48.

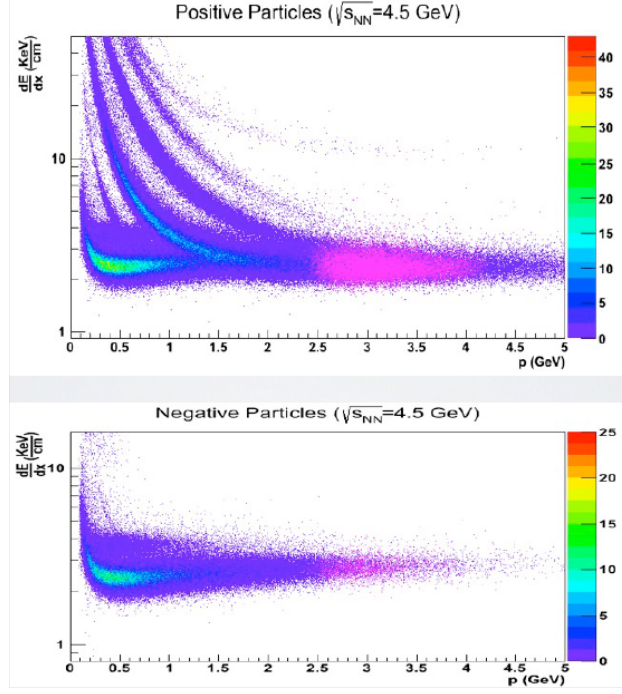FIG. 49.

IX. dE/dx FITS

bf Macro: — fitZTPCPions.C

bf Macro: — fitZTPCProtons.C

bf Macro: — fitnSigmaTPCPionHistograms.C

bf Macro: — fitnSigmaTPCProtons.C

There are two measures of dE/dx that are commonly used in STAR for particle identification, the $n\sigma$ variable and the $zTPC$ variable. This analysis uses both of these variables and this allows for a study of systematic errors. The $n\sigma$ variable is defined as zero for the particle of interest and measures the distance between the dE/dx of a track and the Bichsel Curve of the particle of interest in units of σ. Because energy loss in the TPC is a random process we expect to see Gaussian distributions for each particle species in $n\sigma$ space. The $zTPC$ variable, on the otherhand, is a scaled and offset logrithm of the straight dE/dx. In general, the $n\sigma$ variable produces a better Gaussian distribution for the particle of interest while reducing the quality of distributions of the other particle types. The $zTPC$ variable, does not improve or distort either signal. The $n\sigma$ variable is the best choice in region of momentum space where the particle of interest is well separated from the other particle species, whereas the $zTPC$ variable is the best choice when PID bands are overlapping. This analysis methodology was first developed to look only at the midrapidity slices. We later decided to expand the analysis to try to cover as broad a rapidity range as possible. This expanded rapidity range (which is the topic of another paper) pushed the spectra into regions in which PID became more challenging and therefore we added the $zTPC$ variable analysis methodology.

The tracks are divided into 25 MeV transverse mass bins and their $n\sigma$'s and $zTPC$'s are histogramed. Only tracks within $\pm.5$ units of rapidity from mid-rapidity are considered. Rapidity for all tracks is calcualated assuming each track to be the particle of interest. The histograms are then fit with as many Gaussians as necessary where we have fixed the mean, width, and fit range and permitted the amplitude (labeled as "constant in the plots below) to float. The mean, width, and fit range are fixed to values which result in the best χ^2/ndf value. The Gaussians are then integrated to find the raw yields of the particles of interest.

For the π^- analysis, in the $n\sigma$, we do only single Gaussian fits and ignore the electron contamination. In the $zTPC$ analysis we fit Gaussian to both the π^-'s and the e's. No

28

significant difference is seen for the mid-rapidity spectra. For the π^+ analysis, in the $n\sigma$, we add a second Gaussian fits when the protons start to contaminate the pion yield. In the $zTPC$ analysis we fit Gaussian to the π^+'s, p's, and the e's. No significant difference is seen for the mid-rapidity spectra. For the proton analysis, we use only the $n\sigma$ variable. We first fit the π^-'s that would fall in the anti-proton bins. As there are no anti-protons, this helps to set the π^+ contamination of the protons, however, we also know that the pion ratio is not unity at these energies (that is one of the main points of this paper). We use the pion ratios that we have measured to scale the π^-'s appropriately, and this allows us to completely fix the pion contamination of the proton bins. We add a third Gaussian to account for the deuterons.

FIG. 50. (9.1)

FIG. 51. (9.2)

29
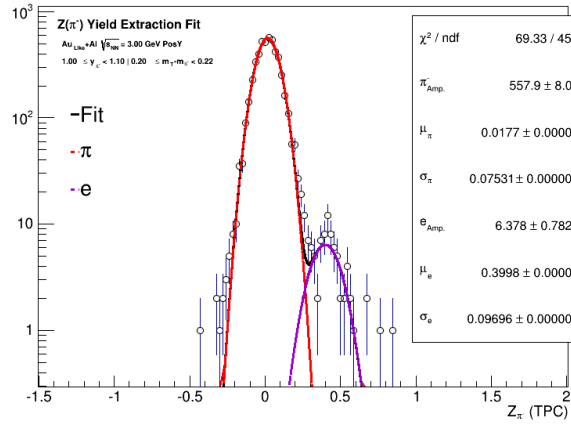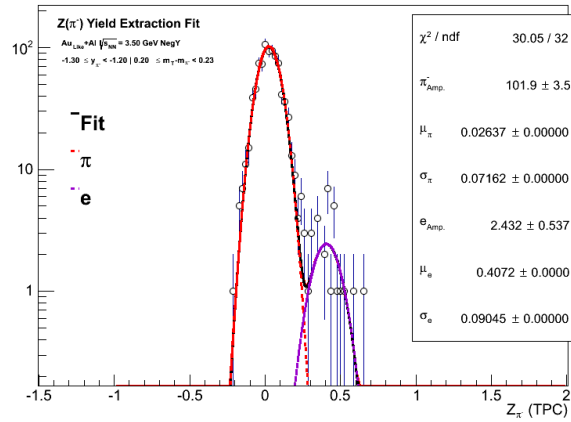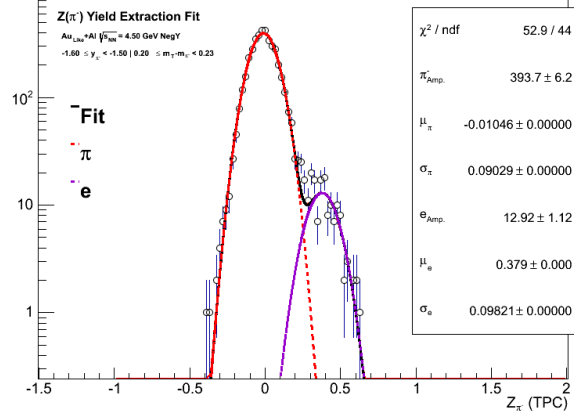
FIG. 52. (9.3)
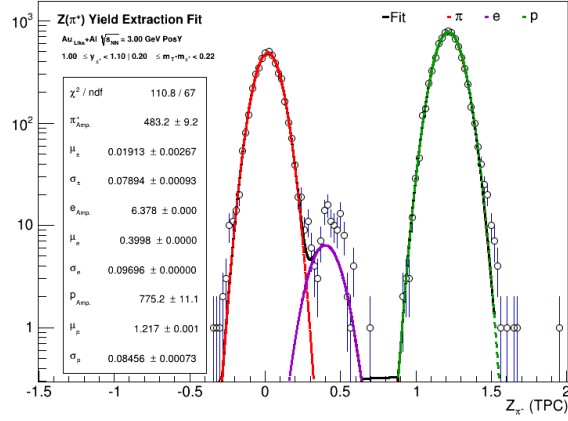
FIG. 53. (9.4)

The full set of fits can be found at: http://nuclear.ucdavis.edu/ star/protected/FixedTargetPaper/analys

As the analysis was done independently with using both the nSigma and the zTPC variable to define the dE/dx, these parallel analyses can be used to determine the systematic error that is introduced at this stage of the analysis. In three figures below show a comparison of the pion spectra extracted using the zTPC variable (solid symbols) and the nSigma variable (open symbols).
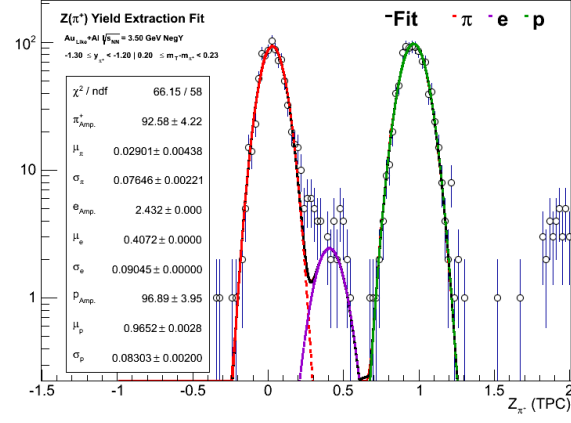
FIG. 54. (9.5)
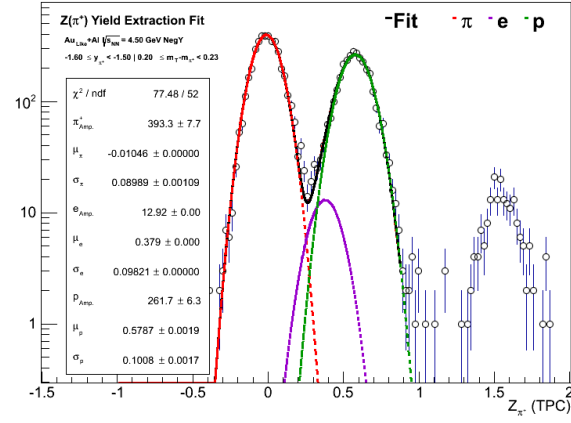
FIG. 55. (9.6)
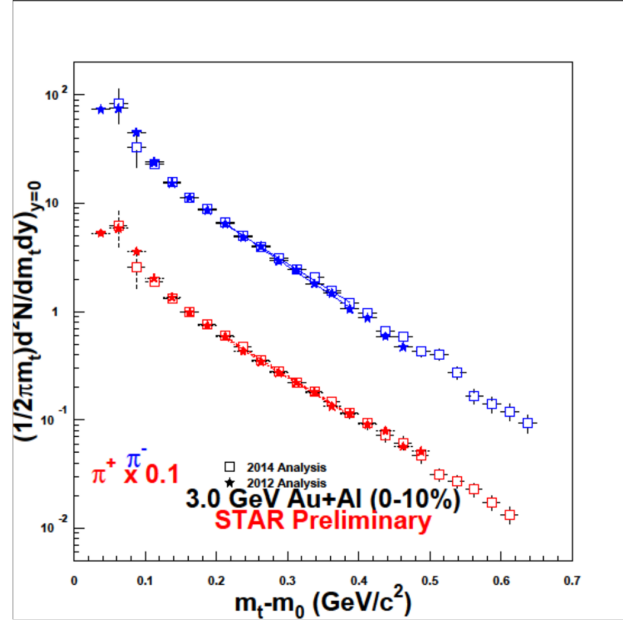
FIG. 56. 9.10
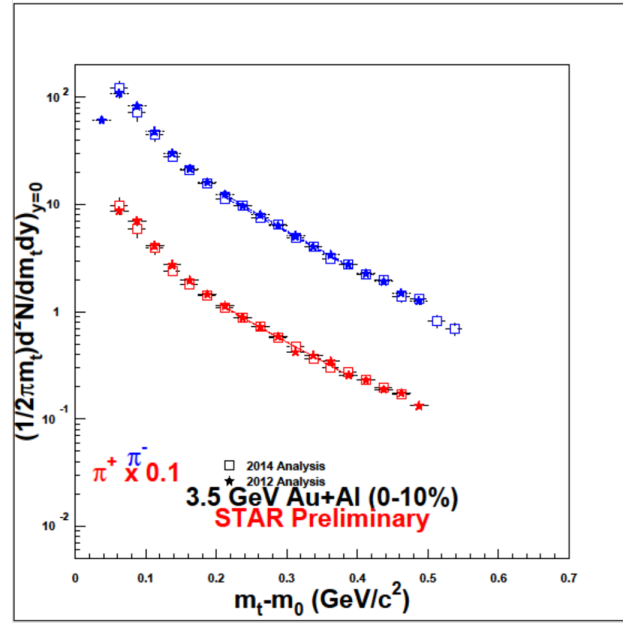
FIG. 57. 9.11
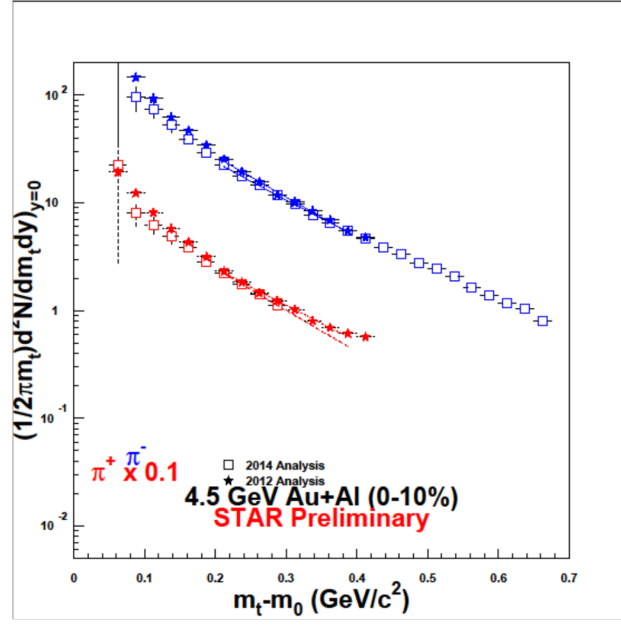
FIG. 58. (9.12)

X. EFFICIENCY CORRECTIONS

bf Macro: — fitEfficiencyCurves.C

The efficiencies are determined using embedding data. The embedding results are fit to an equation with the functional form: $\epsilon = Amplitude * exp^{(m_T - m_0/Slope)^{Power}}$ This function does not do a good job describing the lowest $m_T - m_0$ bins and for these bins we use the embedding results directly. Details of exactly which bins use the functional form and which use the direct embedding results can be found in the .xlsx files are are linked at the bottom of the section.

bf Systematic Errors

Systematic errors in the spectra (which are shown later in Fig.s 12.1 and 12.2) are determined by using the two most important systematics. The pion spectra were determined independently using two different methodologies (see section 9). The differences between the two independent methods produce a 3% systematic (see figures on the web page). The second important systematic comes from the uncertainty in the efficiency corrections. To estimate this systematic, the parameters from the function fit to the embedding data in figures 10.1 to 10.6 are taken to their limits to determine the maximum uncertainty. In additiion, for the low mT-m0 point for the pions, where the functional form does not fit the embedding data, the efficiency results and the uncertainty where used directly from the embedding data. Point-by-point systematics errors can be found in the data files linked below.

FIG. 59. (10.1)

34
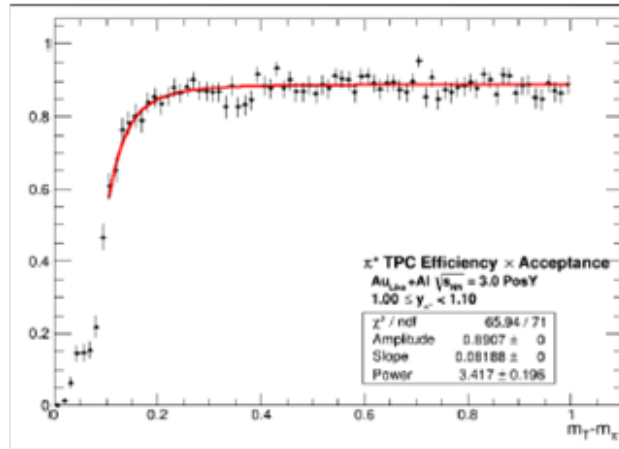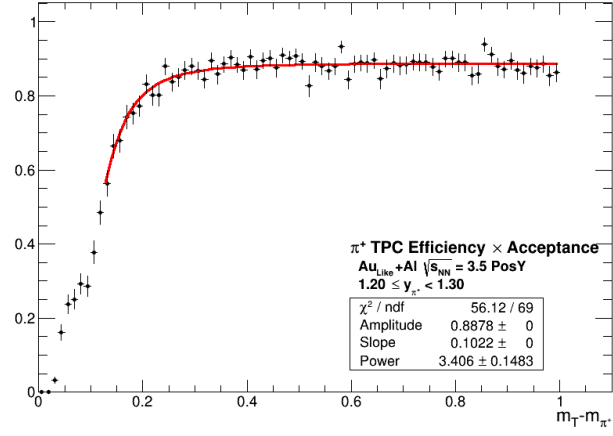
FIG. 60. (10.2)
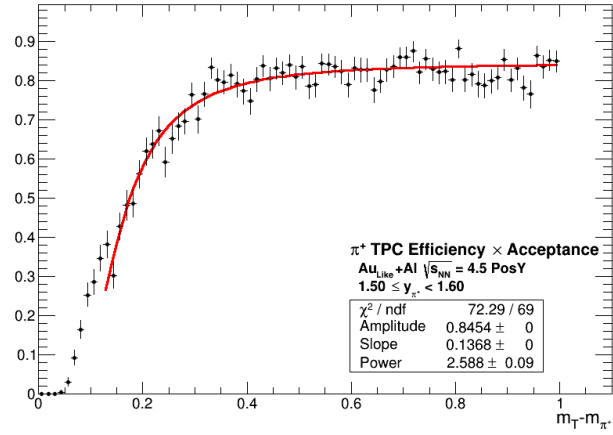
FIG. 61. (10.3)

FIG. 62. (10.4)

35
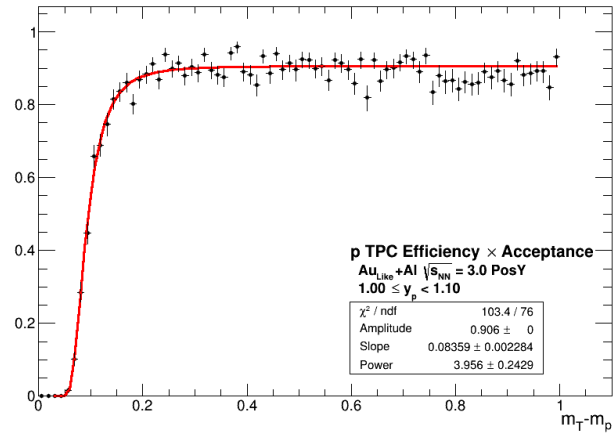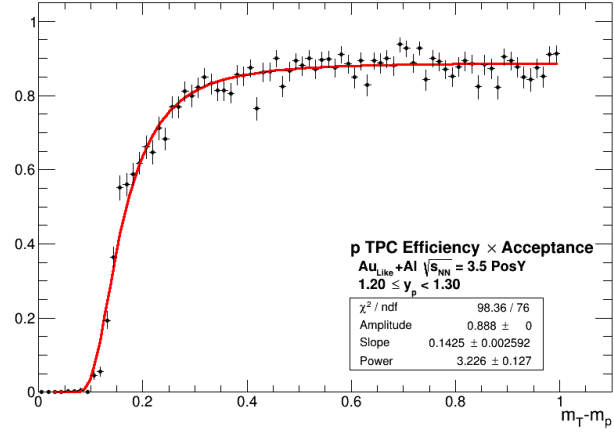
FIG. 63. (10.5)
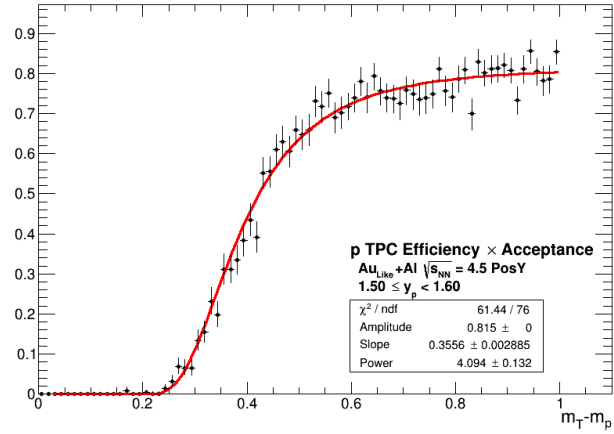
FIG. 64. (10.6)

XI. ENERGY LOSS CORRECTIONS

bf Macro: — fitEnergyLossCurves.C

The embedding data can also be used to estimate the energy lost by a track prior to it reaching the tracking volume of the TPC. The tracking software assumes every track to be a pion and there is an attempt made to correct each track for the energy lost in the beam pipe and the inne field cage of the TPC (the BES runs were very low mass runs which a minimum of material between the interaction point and the TPC). The embedding data can be used to estimate how well the tracking software is able to make this correction. The macro compares the initial momentum of the embedded track to the reconstructed momentum. AS can be seen in the top row of plots below, the energy loss correction for points is extremely small.

The protons loose more energy in the material than the pions, and the software correct assumes that every track in a pion, so in general the energy loss correction in more important for protons. This is evident when one compares the scales of the pion corrections on the top row below with those for the proton corrections on the bottom row. These corrections are applied, however they are far less effect on the proton spectra than the efficiency corrections outlined in the previous section.

The energy loss correction is extremely small. Therefore the systematic error associated with this correction is not significant.

FIG. 65. (11.1)

37
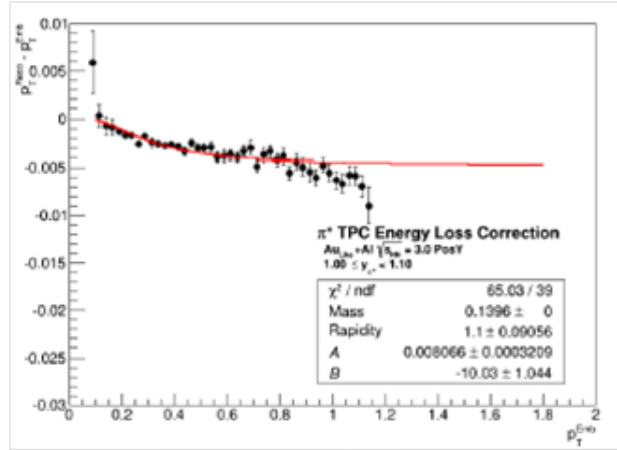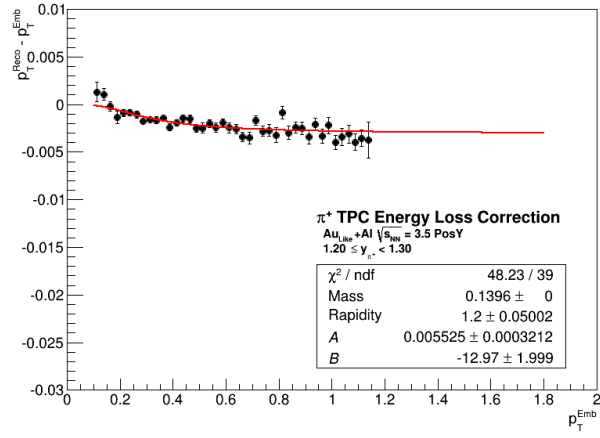
FIG. 66. (11.2)
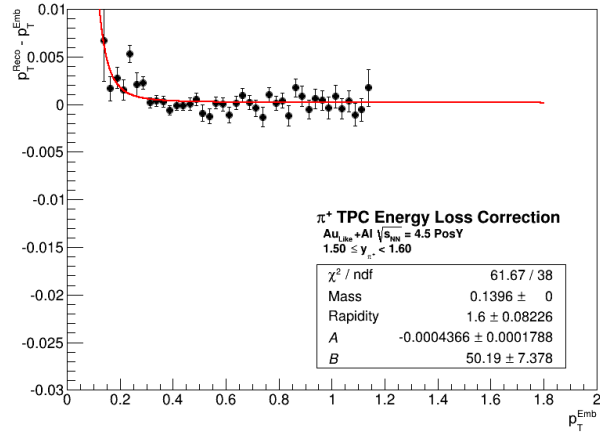
FIG. 67. (11.3)

FIG. 68. (11.4)

38
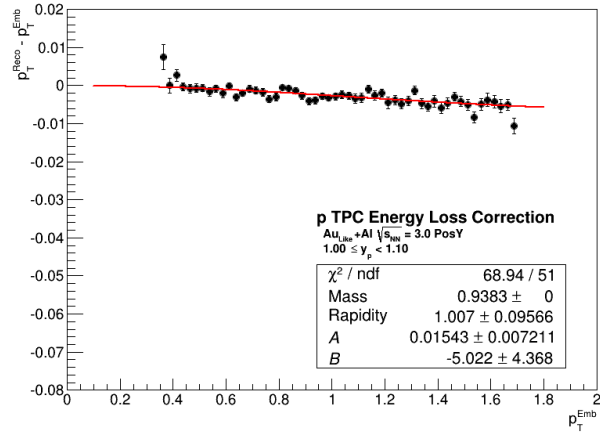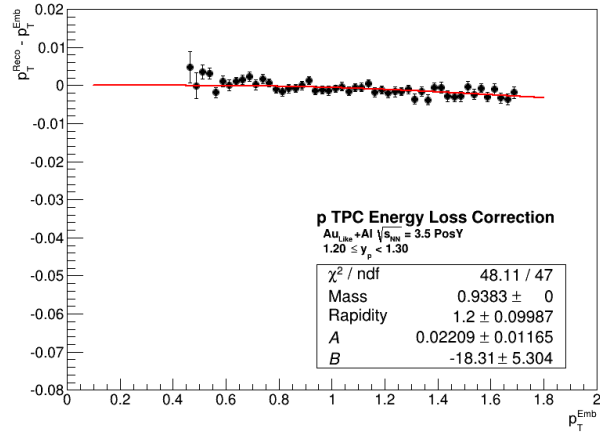
FIG. 69. (11.5)
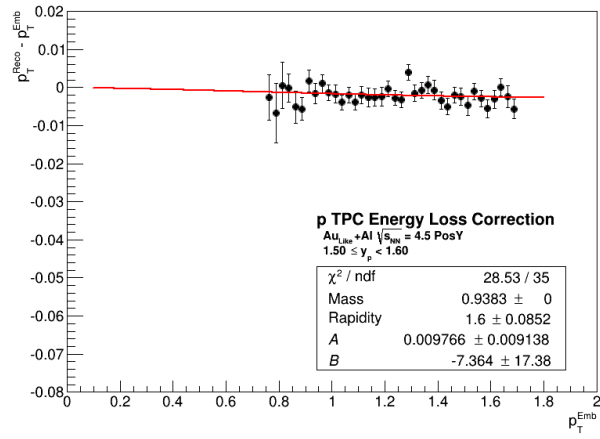
FIG. 70. (11.6)

XII.   INVARIANT PARTICLE SPECTRA

bf Macro: — doSpectraCorrections.C

bf Macro: — doSpectraFitsAnddNdy.C

The raw yields are converted to an invariant yield by dividing by $1/(2\pi m_T)$ and the efficiency (ϵ), then normalizing with respect to the transverse mass (dm_T) and rapidity (dy) bins and the number of events (N_{Evt}). The slope parameters of the spectra are required for the subsequent Coulomb potential fit of the pion ratio. The pion spectra are fit from 200 to 400 MeV/c^2 with an Bose-Einstein function $f(m_T - m_0) = (dN/dy)A/(e^{m_T/T} - 1.0)$ where A is the integral of $1.0/(e^{m_T/T} - 1.0)$ from zero to infinity. The proton spectra are fit with exponential function in their respective across the full measured range to extract the slope parameters. We fit the proton spectra with the functional form

$$f(m_T - m_0) = \frac{dN}{dy} \frac{m_T}{2\pi T(m_0^2 + 2m_0 T + 2T^2)} e^{\frac{m_T}{T}} \tag{2}$$

where the particle yield per unit rapidity, $\frac{dN}{dy}$, and the slope parameter, T, are fit parameters, m_T is the particle's transverse mass, and m_0 is the particle's rest mass

bf Systematic Errors:

The systematic errors in the data points shown in figures 12.1 and 12.2 are determined by combining the two most important systematics. The yields of the individual points were independently determined using two different methodologies, which are outlined in section 9. The systematic differences in these two methodologies results in 3% systematic error. The systematic from the efficiency calcualtion was determined by taking taking the parameters of the function fit to the embedding data to their limits. This results in a systematic error also of about 3%. For the low mT-m0 efficiency points, the fit function fails and the embedding results and their range were used directly. Point-by-point details of the systematic errors are available in the data files.

Systematic errors in the inverse slope parameters (T) and rapidity densities (dN/dy)are determined by varying the fit ranges over which the spectra are fit. These errors are detailed in the table below.
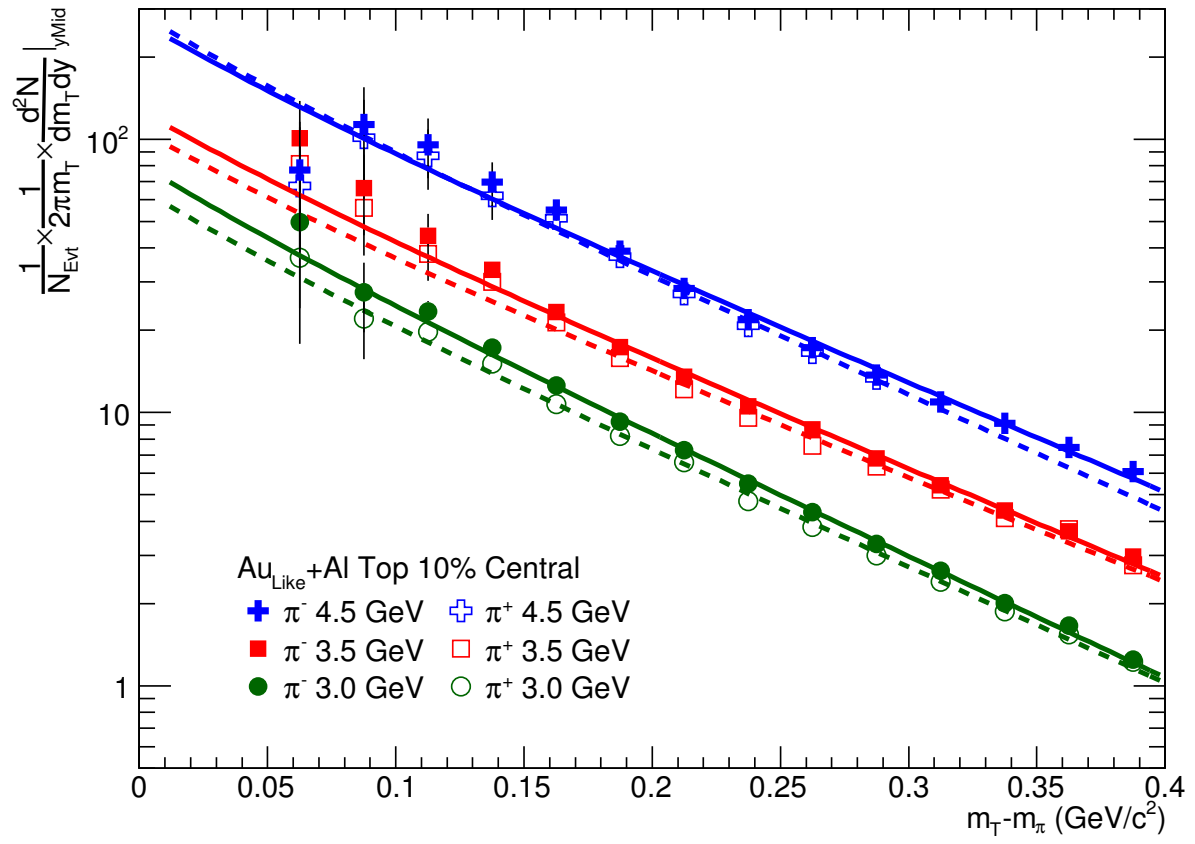
FIG. 71. (12.1)
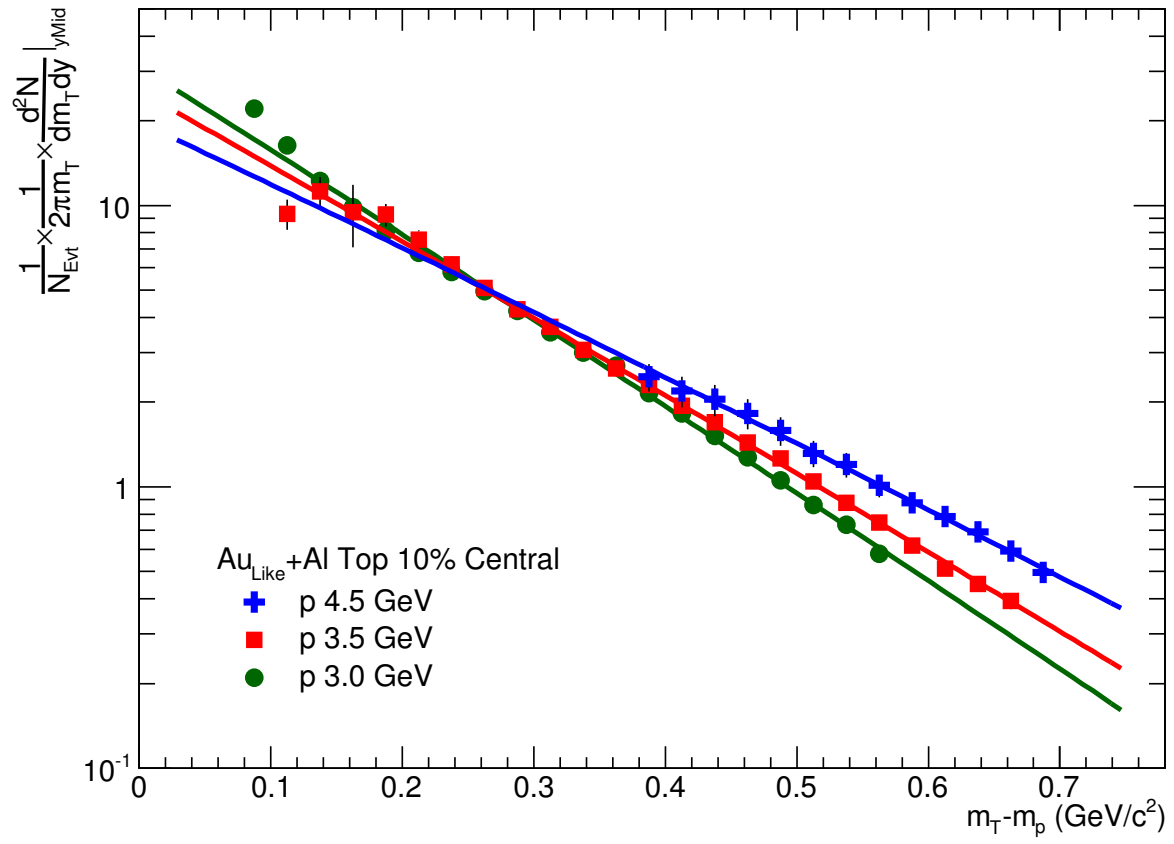
FIG. 72. (12.2)

TABLE III. (12.1) The T values are the inverse slope parameters describing the pion and proton spectra. The $\mathrm{d}N/\mathrm{d}y$ values are the rapidity densities measured at y_{CM} in $Au_{like} + Al$ at $\sqrt{s_{NN}} = 3.0$, 3.5, and 4.5 GeV. Statistical and systematic errors are listed.

$\sqrt{s_{NN}}$ (GeV)	particle	T (MeV)	$\mathrm{d}N/\mathrm{d}y|_{y=0}$
	π^+	$103 \pm 3 \pm 5$	$8.7 \pm 0.3 \pm 0.5$
3.0	π^-	$99 \pm 3 \pm 3$	$10.1 \pm 0.3 \pm 0.3$
	p	$128 \pm 2 \pm 6$	$30.7 \pm 0.5 \pm 5$
	π^+	$115 \pm 3 \pm 9$	$16.1 \pm 0.5 \pm 0.6$
3.5	π^-	$111 \pm 3 \pm 8$	$18.2 \pm 0.6 \pm 1.0$
	p	$141 \pm 2 \pm 3$	$28.4 \pm 0.7 \pm 5$
	π^+	$102 \pm 8 \pm 10$	$38 \pm 5.1 \pm 4$
4.5	π^-	$110 \pm 4 \pm 6$	$37 \pm 1.7 \pm 2$
	p	$164 \pm 6 \pm 7$	$27 \pm 2.5 \pm 5$

XIII.   PION RATIOS

Macro: — doPionRatios.C

The above macro is used to fit the pion ratio plots for the 3.0 (Green), 3.5 (Red) and 4.5 GeV (Blue) $Au + Al$ systems. This macro uses the Coulomb formulas which are detailed in the paper (and in the graphic below) in equations (1) through (4). The slope parameters for the pions (T_π) an protons (T_p) are determined by the fits to the spectra which are detailed in the previous section. The Coulomb fit therefore have only two free parameters, the Coulomb Potential (V_C) and the initial pion ratio (R_i). The pion ratio data (solid stars) and the Coulomb fit functions (solid lines) are shown in figure 13.1 below. The data points for the pion ratio fits are taken without systematic error because all systematics cancel when taking the ratio as all systematics will effect π^- and π^+ equally.

Systematic Errors:

Systematic errors in the final extracted values for V_C and R_i are determined by varying the range over which the pion ratio data are fit. These fits over varied ranges are shown in Figures 13.2 through 13.10. The standard deviation of the fit values across the three different fitting ranges is taken as the systematic error of the measurement.

TABLE IV. (13.1) The extracted Coulomb potential (V_C) and initial pion ratio (R_i) are tabulated for each bombarding energy. Statistical and systematic errors are listed.

$\sqrt{s_{NN}}$ (GeV)	$V_C|_{y=0}$ (MeV)	$R_i|_{y=0}$
3.0	$12.1 \pm 1.1 \pm 1.5$	$0.81 \pm .06 \pm .08$
3.5	$9.1 \pm 0.9 \pm 0.6$	$0.85 \pm .05 \pm .03$
4.5	$7.5 \pm 1.5 \pm 1.9$	$0.90 \pm .07 \pm .03$

FIG. 73. (13.1)

FIG. 74. (13.2)

FIG. 75. (13.3)

FIG. 76. (13.4)

FIG. 77. (13.5)

FIG. 78. (13.6)

FIG. 79. (13.7)

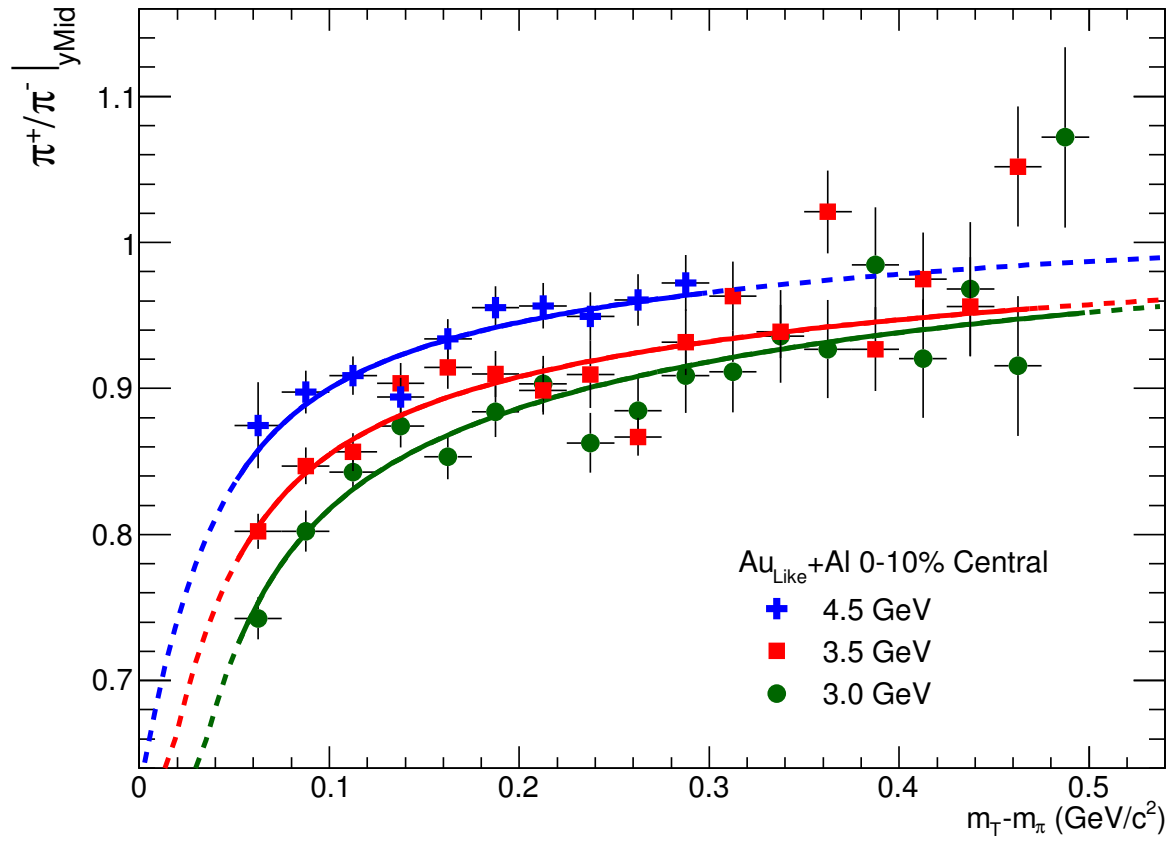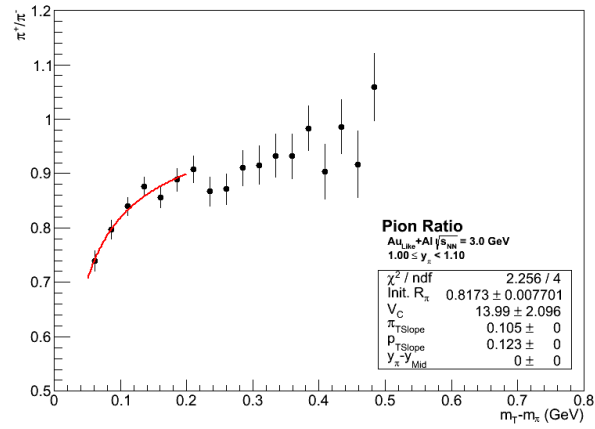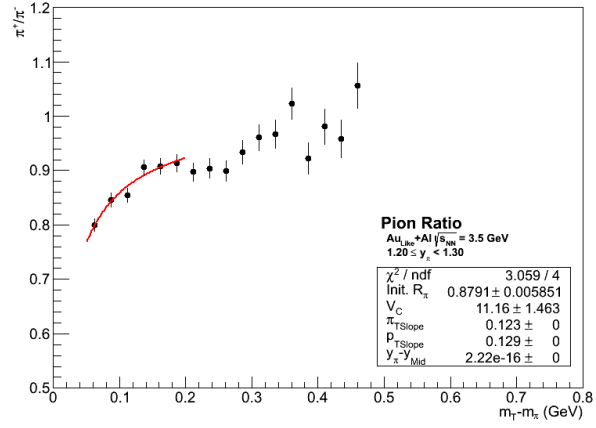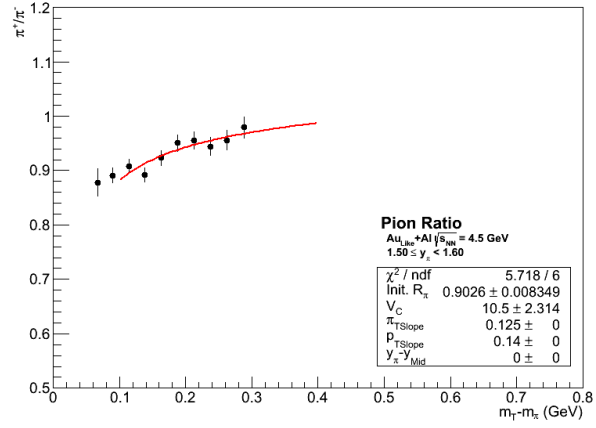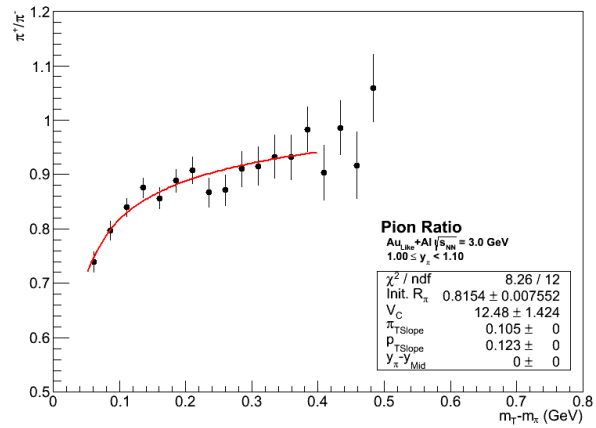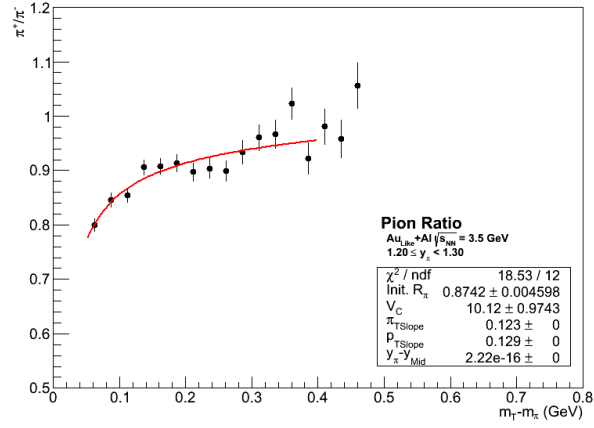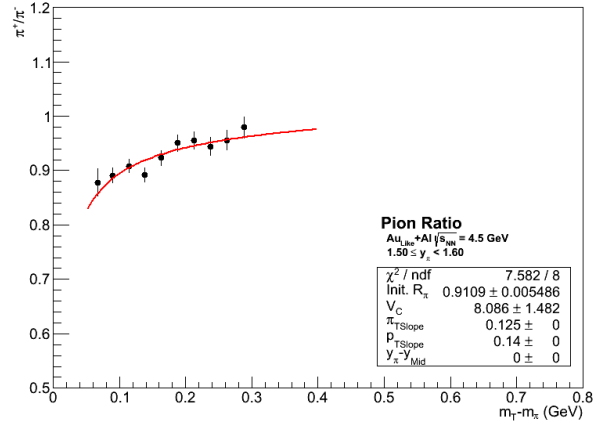FIG. 80. (13.8)

47
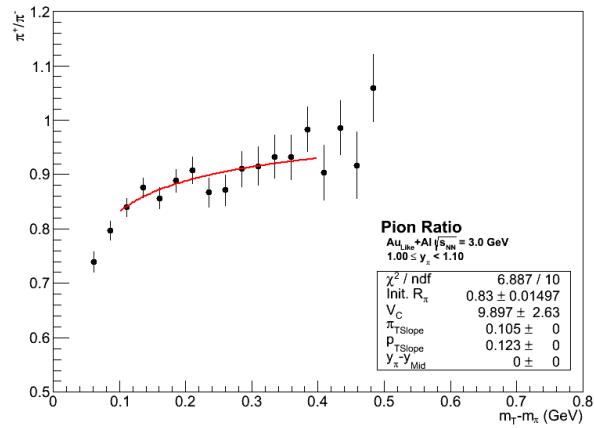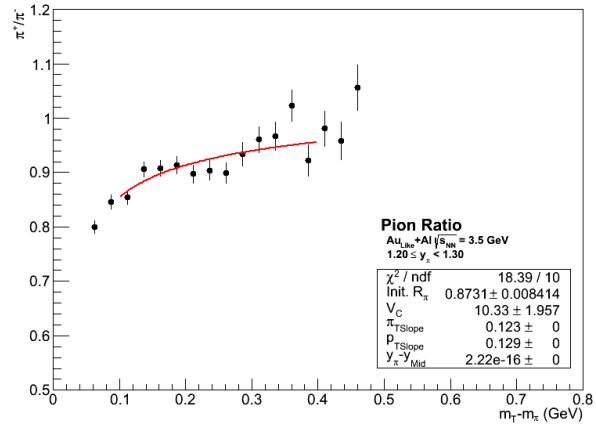
FIG. 81. (13.9)
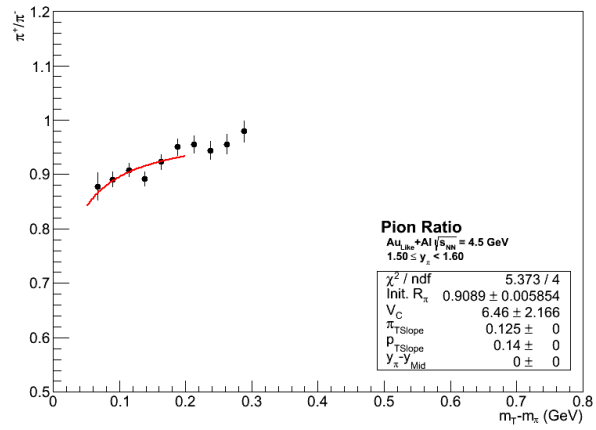
FIG. 82. (13.10)

XIV. VC TRENDS

The Coulomb potential analysis that was outlined in the previous section provides a very straight forward analysis to make an experimental measurement of the Coulomb potenital experienced by the pions as they are emitted from the interaction region. Interpreting what this Coulomb potential means does require some assumptions of the geometry and dynamics of the reaction. However if we just fall back onto the simplest concepts and don't try to overinterpret the results we can draw rather interesting conclusions about these reactions. We all recall from introductory physics that the Coulomb Potential for a point charge is given by: $V_C(r) = Q/(4\pi\epsilon_0 r)$ where Q is the charge, r is the radius, and ϵ_0 is the permittivity of free space. We also know from Gauss' law, that for a distribution of charges, we are only concerned with the charges which are at a radius smaller than r. Basically this means that we are concerned with the positive charge (i.e. protons) which is exiting the interaction region slower than the pions and the radius at which the pions are emitted.

In Fig. 14.3 we show the collision energy systematics of our extracted V_C values. The $Au_{like} + Al$ data are shown as solid red stars. One notes that the V_C values are dropping with energy. This can mean that the emission radius is increasing, the charge of the source is decreasing, or both are changing. To try to get a handle on which of these might be the most likely cause for the reduction in V_C with collision energy, we compare our new $Au_{like} + Al$ results to values of V_C extracted from a similar analysis to the published pion spectra from central $Au + Au$ and $Pb + Pb$ collisions (shown as mostly open symbols in Fig. 14.3). This not such a great comparison set, but most of the good published results are from central collisions of the heaviest ions. we note that the V_C values for the heavy systems are always systematically higher than those for the $Au_{like} + Al$ data sets. This is not surprising. Assuming a spherical static source with the charge given by the number of participating protons in the overlap region and the emission radius given by the size of the overlap region (both participating protons and size of the overlap region are found with a Glauber model), the expected Coulomb potential for $Au + Au$ collisions would be: $V_C(Au + Au) = 136e/(4\pi\epsilon_0 7.0 fm) = 28.0$ MV For Comparison, the expected Coulomb potential for $Au + Al$ collisions would be: $V_C(Au + Au) = 35e/(4\pi\epsilon_0 3.4 fm) = 14.8$ MV First we note that this "limit" falls quite close to the values of V_C found for $Au + Au$ collisions at $\sqrt{s_{NN}} = 2.2$ GeV. We know that as the beam energy is increased above 1 AGeV ($\sqrt{s_{NN}} = $

49

2.2 GeV), we start to see a reduction in stopping as the nucleons develop transparency to one another. There are several different ways to define and quantify stopping, but for the purposes of this argument will we use the mid-rapidity dN/dy of net-protons as a measure of stopping. This is a useful measure for the Coulomb analysis because we are concerned with how much positive charge is left in the interaction region. The midrapidity dN/dy of net-protons can be used as a proxy for the charge of the interaction region. In order to have a value that can be compared from experiment to experiment, then dN/dy values have been scaled by the average number of participants that each experiment estimated for their most central data selections. These data are plotted on the figure as open blue symbols. To get a sense of the reduction in stopping with increased collision energy, we fit these dN/dy data with a falling exponential. $y(x) = Ae^{-x/T}$ We find $A = 45.86$ and $T = 1.595$. This is an empirical fit. We do not mean to imply any physics, we simply need a way to characterize the stopping.

We note that the open black (V_C) and blue (dN/dy) symbols seem to track one another. This implies that the change in Coulomb potential is due to a reduction in the charge of the interaction region and not due to expansion. More importantly for this fixed target paper, this empirical fit can be used to predict where one would expect a $Au + Al$ system to fall. We take the functional form found in the blue solid curve and first scale by 100 to convert dN/dy to MV (this is another impirical conversion factor... there is noting magic about 100, it just turns out that way); then we scale by $(35e/136e)(7fm/3.4fm)$. This gives us the dashed red curve. This is a prediction of the expected V_C values for $Au + Al$ systems assuming that the stopping in $Au + Al$ is comparable to the stopping in $Au + Au$. This dashed red curve is not a fit. It is a prediction. The fact that it is consistent with the data implies that the charge of the projectile is similar to that of gold.

But the previous comparison is made by scaling the trends from heavier systems. We want to try to see if that scaling makes sense. We have search the literature for pion spectra from lighter systems and found several interestng data sets for the heavy ion program at SIS. First we present the Coulomb potential analysis for pion spectra results from FOPI for $Ru + Ru$ at 0.4 and 1.528 AGeV and $Ni + Ni$ at 1.06, 1.45, and 1.93 in Fig. 14.1. In Fig. 14.2 we show the Coulomb analysis of pion spectra data from HADES for $Ar + KCl$ at 1.76 AGeV and $C + C$ at 1.0 and 2.0 AGeV. There exist data from KaoS for $C + C$ and $C + Au$ at 1.8 AGeV, but we have not been able to acquire those data yet.

¹ An extremely important comparison data set for pions ratios is available from E802 for
² 14.6 AGeV $Si + Au$. Since this system is analogous to the $Au + Al$, this comparison is very
³ important. They Coulomb analysis of this system is shown in Fig. 14.2. For these lighter
⁴ systems, we estimate the average number of participant protons (Q) and the average radius
⁵ of the overlap volume (r_O) using the centrality estimates of the collaborations and a Glauber
⁶ model. Using $Qe/(4\pi\epsilon_0 r_O) = V_C$, we get the following expected Coulomb potentials for fully
⁷ stopped systems (i.e. 1 AGeV):

TABLE V. (14.1) V_C for fully stopped systems

System	Q (e)	r_O (fm)	V_C (MeV)
$C + C$	10	2.8	5.2
$Ar + KCl$	30	4.1	10.5
$Ni + Ni$	48	4.9	14.1
$Ru + Ru$	79	5.6	20.3
$Au + Al$	35	3.4	14.8
$Au + Au$	136	7.0	28.0
$Pb + Pb$	141	7.2	28.2

⁸ The results of the Coulomb potential analysis on the lighter systems is shown in colored
⁹ plotting symbols on Fig. 14.3. The expectations based on the $Au + Au$ trend line are shown
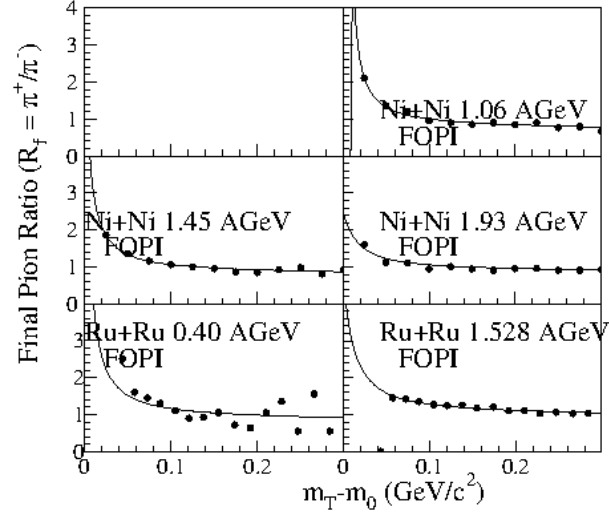¹⁰ on Fig. 14.3 as colored dashed lines.
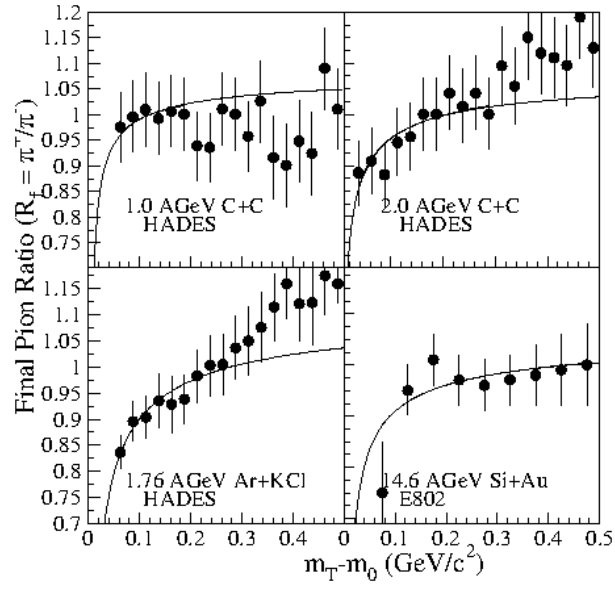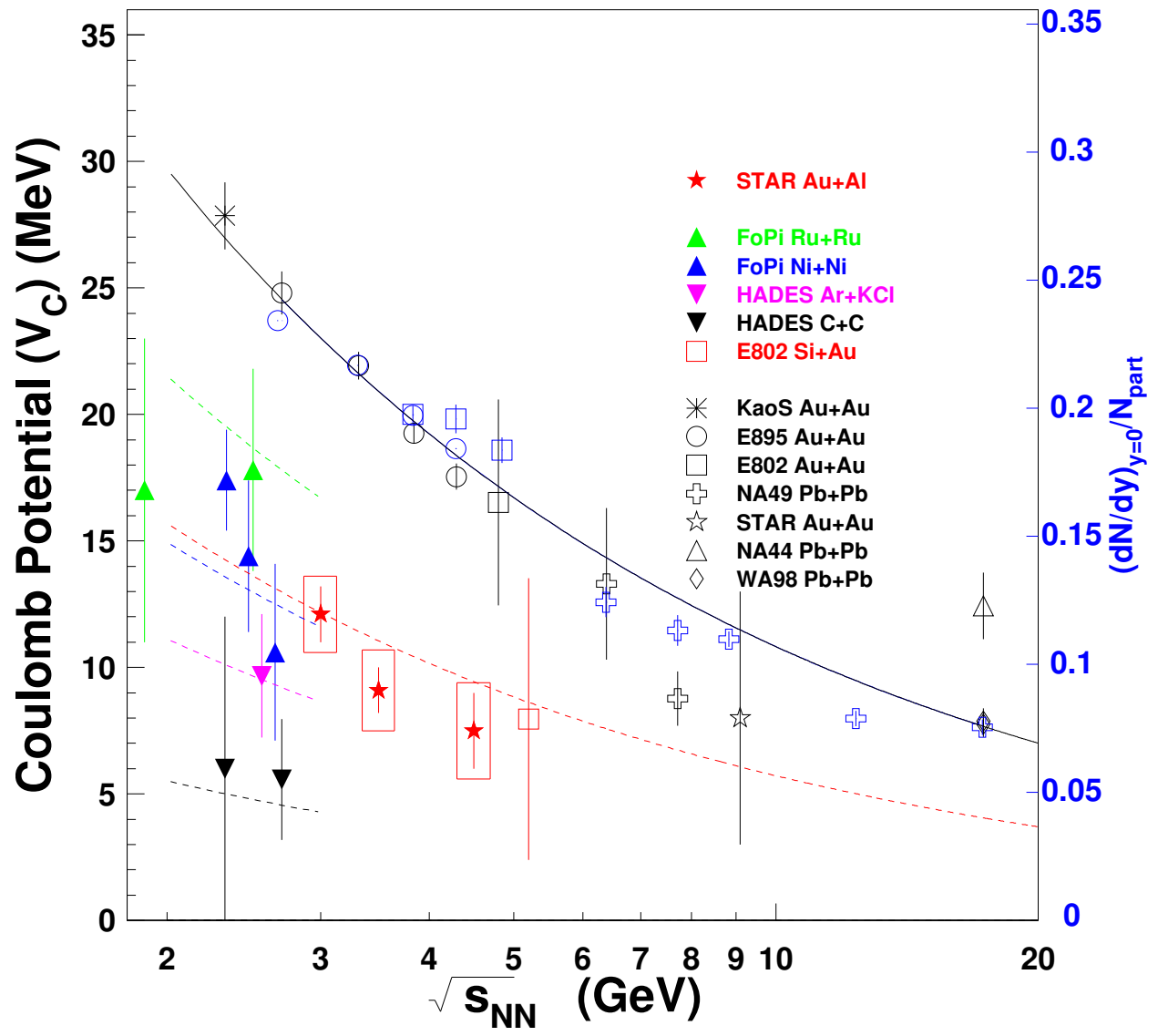
FIG. 83. (14.1)

FIG. 84. (14.2)

FIG. 85. (14.3)

XV. RI TRENDS

At the top energies of STAR, we generally assume that the number of π^+'s and π^-'s are equal, and at $\sqrt{s_{NN}} = 200$ GeV you are pretty close to being right. But at lower energies for heavy systems there is a preference for production of π^-'s. This is because at the lowest energies almost all pions are produced through Δ resonance channels, while as one increases the collision energy a larger and larger fraction of pions are produced directly as pairs of pions (hence no preference for one charge over the other).

So let us start this discussion by posing the question, "what would the pion ration be if all pions were created in first chance NN collisions that proceed through the Δ resonance?" Here we combine our knowledge of the relative frequencies of various reaction channels based on the isospin combinations of the entrance and exit channels with the experiementally determined pion production cross-sections at energies below 1.5 AGeV compiled by B.J. VerWest and R.A. Arndt, PRC25, 1979 (1982). First we will break down the crossections for the various processes, then we will consider the relative rates for the various channels to ultimately determine the expected ratio of π^+/π^-, assuming all pion production proceeds through the Δ resonance channel.

TABLE VI. (15.1)

Reaction Channel	cross section
$p + p \rightarrow n + \Delta^{++} \rightarrow n + (p + \pi^+$	16 mb
$p + p \rightarrow p + \Delta^+ \rightarrow p + (n + \pi^+$	2 mb
$p + p \rightarrow p + \Delta^+ \rightarrow p + (p + \pi^0$	4 mb
$p + n \rightarrow n + \Delta^+ \rightarrow n + (p + \pi^0$	4 mb
$p + n \rightarrow n + \Delta^+ \rightarrow n + (n + \pi^+$	2 mb
$p + n \rightarrow p + \Delta^0 \rightarrow p + (p + \pi^-$	2 mb
$p + n \rightarrow p + \Delta^0 \rightarrow p + (n + \pi^0$	4 mb
$n + n \rightarrow n + \Delta^0 \rightarrow n + (n + \pi^0$	4 mb
$n + n \rightarrow n + \Delta^0 \rightarrow n + (p + \pi^-$	2 mb
$n + n \rightarrow p + \Delta^- \rightarrow p + (n + \pi^-$	16 mb

Having established the cross sections for the various reactions that lead to pion production through an intermediate Δ, we now need to estimate the relative rate for the various NN

collisions. Let us first consider $Au + Au$ reactions. Using simple Glauber model using a 40 mb total NN cross section, one estimated 354 participating nucleons in a central $Au + Au$ collision, which breaks down to 68 protons and 109 neutrons from each nucleus. We can use these to estimate the realtive numbers of π^+ and π^-.

TABLE VII. (15.2)

Reaction	Contributions	Yield
$p + p \rightarrow n + p + \pi^+$	68 x 68 x 18 mb	83232 mb
$p + p \rightarrow p + p + \pi^0$	68 x 68 x 4 mb	18496 mb
$p + n \rightarrow n + n + \pi^+$	68 x 109 x 2 x 2 mb	29648 mb
$p + n \rightarrow n + p + \pi^0$	68 x 109 x 2 x 8 mb	118592 mb
$p + n \rightarrow p + p + \pi^-$	68 x 109 x 2 x 2 mb	29648 mb
$n + n \rightarrow n + n + \pi^0$	109 x 109 x 4 mb	47524 mb
$n + n \rightarrow n + p + \pi^-$	109 x 109 x 18 mb	213858 mb

Our total yield of π^+ is $83232 + 29648 = 112880$ mb, while our total yield of π^- is $29648 + 213858 = 243506$ mb. This predicts that $\pi^+/\pi^- = 112880/243506 = 0.4636$. We see in Fig. 15.1 that this value is quite close to the pion ratio value extracted from analyzing the KaoS data at 1 AGeV ($\sqrt{s_{NN}}$=2.33 GeV). The figure also shows R_i values extracted from $Au + Au$ and $Pb + Pb$ data sets for a range of collision energies from 2.33 to 20 GeV. We note that the R_i values increase with collision energy. We can make a simple ansatz that pion the cross section to pion production through the $Delta$ channel does not change with collision energy, however new channels which are isospin independent open and their cross sections rise linearly with $\log \sqrt{s_{NN}}$. This is not a bad assumption as it has not noted that the dN/dy for pions is seen to increase linearly with the log of the collision energy. The black solid curve on Fig. 15.1 follows the functional form: $R(x) = (0.4636 + A(log(x) - log(2.33)))/(1.0 + A(log(x) - log(2.33)))$ where x is $\sqrt{s_{NN}}$, and A is the fit variable which describes the linear increase in isopsin independent pion production. In this analysis it is found that $A = 1.636$.

Having established the systematics of the R_i for collisions with the heaviest ions, we can now ask where we would expect the curve to fall for $Au + Al$ collisions. We again use a Glauber model to determine the number of particpating protons and neutrons (the results

have already been shown in section 6, are repeated here.

TABLE VIII. (15.3) Participating nucleons

3.0 GeV	3.5 GeV	4.5 Gev
Npart = 80.35 ± 0.10	Npart = 82.32 ± 0.09	Npart = 82.74 ± 0.08
Nprot-Al = 13	Nprot-Al = 13	Nprot-Al = 13
Nneut-Al = 14	Nneut-Al = 14	Nneut-Al = 14
Nprot-Au = 21	Nprot-Au = 22	Nprot-Au = 22
Nneut-Au = 32	Nneut-Au = 33	Nneut-Au = 33

We can now use these estimates of participants to predict the pion ratio for $Au + Al$ collisions at 2.33 GeV.

TABLE IX. (15.4)

Reaction	Contributions	Total Yield
$p + p \rightarrow n + p + \pi^+$	13 x 22 x 18 mb	5148 mb
$p + p \rightarrow p + p + \pi^0$	13 x 22 x 4 mb	1144 mb
$p + n \rightarrow n + n + \pi^+$	(13 x 33 + 14 x 22) x 2 mb	1474 mb
$p + n \rightarrow n + p + \pi^0$	(13 x 33 + 14 x 22) x 8 mb	5896 mb
$p + n \rightarrow p + p + \pi^-$	(13 x 33 + 14 x 22) x 2 mb	1474 mb
$n + n \rightarrow n + n + \pi^0$	14 x 33 x 4 mb	1848 mb
$n + n \rightarrow n + p + \pi^-$	14 x 33 x 18 mb	8316 mb

Our total yield of π^+ is 5148 + 1474 = 6622 mb, while our total yield of π^- is 1474 + 8316 = 9790 mb. This predicts that $\pi^+/\pi^- = 6622/9790 = 0.6764$. The red dashed curve is then a prediction using the functional form: $R(x) = (0.6764 + A(log(x) - log(2.33)))/(1.0 + A(log(x) - log(2.33)))$

Comparisons are also made for the same lighter systems considered in the previous section. The data points are shown on Fig. 15.1 with colored plotting symbols. The expectations, shown in the table below for 1 AGeV, are shown as colored dashed curves illustrating the expected trend lines for all lighter systems.

TABLE X. (15.5)

System	N_p	N_n (fm)	R_i (MeV)
$C + C$	6	6	1.000
$Ar + KCl$	18	20	0.812
$Ni + Ni$	28	32	0.804
$Ru + Ru$	44	52	0.655
$Au + Au$	79	118	0.469

FIG. 86. (15.1)